A generalised finite difference scheme based on compact integrated radial basis function for flow in heterogeneous soils

D. Ngo-Cong[a,*], C.M.T. Tien[a], T. Nguyen-Ky[a], D.-A. An-Vo[a],
N. Mai-Duy[a,b], D.V. Strunin[a,c], T. Tran-Cong[a,b]

[a]*Computational Engineering and Science Research Centre, University of Southern Queensland, Toowoomba, QLD 4350, Australia.*
[b]*School of Mechanical and Electrical Engineering, Faculty of Health, Engineering and Sciences, University of Southern Queensland, Toowoomba, QLD 4350, Australia.*
[c]*School of Agricultural, Computational and Environmental Sciences, Faculty of Health, Engineering and Sciences, University of Southern Queensland, Toowoomba, QLD 4350, Australia.*

Abstract

In the present paper, we develop a generalised finite difference approach based on compact integrated radial basis function (CIRBF) stencils for solving highly nonlinear Richards equation governing fluid movement in heterogeneous soils. The proposed CIRBF scheme enjoys a high level of accuracy and a fast convergence rate with grid refinement owing to the combination of the integrated RBF approximation and compact approximation where the spatial derivatives are discretised in terms of the information of neighbouring nodes in a stencil. The CIRBF method is first verified through the solution of ordinary differential equations, 2–D Poisson equations and a Taylor-Green vortex. Numerical comparisons show that the CIRBF method outperforms some other methods in the literature. The CIRBF method in conjunction with a rational function transformation method and an adaptive time-stepping scheme is then applied to simulate 1–D and 2–D soil infiltrations effectively. The proposed solutions are more accurate and converge faster than those of the finite different method employed with a second-order central difference scheme. Additionally, the present scheme also takes less

---

*Corresponding author. Tel.: +61 414 694 019
  Email address: Duc.Ngo@usq.edu.au (D. Ngo-Cong)

time to achieve target accuracy in comparison with the 1D-IRBF and HOC schemes.

1. Introduction

The fluid movement in unsaturated soils has been widely modelled by the nonlinear Richards equation. This nonlinear equation can be linearised by using either Picard or Newton iterative schemes. Celia et al. [1] proposed a modified Picard approximation based on the mixed form of Richards equation to obtain an accurate solution with improved mass balance. However, the method requires large computational time when solving problems with very dry initial conditions [2]. To overcome this issue, Kirkland et al. [2] developed a transformed Richards equation where a new variable φ is defined as a linear function of pressure head h in saturated or near saturated soils and a linear function of water content θ in unsaturated soils. Pan and Wierenga [3, 4] proposed another transformation method, namely rational function transformation (RFT) method, for simulating 1–D and 2–D infiltration into very dry heterogeneous soils. The spatial discretisation for Richards equation has been carried out using several techniques, such as the finite different method [1], finite element method [1, 5], and finite volume method [6, 7, 8]. Caviedes-Voullième et al. [8] investigated the performance of finite volume schemes in simulating 1–D flows in porous media. Like Celia et al. [1], they also found that the schemes based on the mixed form are accurate and conservative while the ones based on the pressure form are inaccurate and non-conservative.

In recent decades, some mesh-free and radial basis function (RBF)-based methods have been developed for solving partial differential equations (PDEs). The RBF-based methods are capable of universal approximation and those based on mutiquadric (MQ) and Gaussian functions can offer an exponential rate of convergence [9]. Kansa [10] first introduced a collocation method based on MQ-RBFs to solve partial differential equations (PDEs) and showed that the MQ scheme yields an excellent interpolation for different functions over both gridded and scattered data. As an alternative to the conventional differentiated radial basis function network (DRBFN) method [10], Mai-Duy and Tran-Cong [11] proposed an integrated RBFN method (IRBFN) for the

solution of PDEs. Instead of conventional differentiation, they used integration to construct the RBF approximations which significantly improved the stability and accuracy of the numerical solution. Mai-Duy and Tanner [12] presented a one-dimensional integrated radial basis function network (1D-IRBFN) collocation method for the solution of second- and fourth-order PDEs. In this method, IRBFNs are employed to obtain the expressions for the field variable and its relevant derivatives along a grid line. Cartesian grids were used to represent both rectangular and non-rectangular problem domains, resulting in significant efficiency as the computational cost almost negligible in comparison with that required for a body-fitted mesh.

However, global RBF-based methods are not suitable for solving large-scale problems because they produce very dense system matrices [13]. Some researchers have proposed local and compact local RBF-based methods in both the differentiation (e.g. [14, 15, 16, 17, 18, 19, 20, 21, 22]) and integration (e.g. [23, 24, 25, 26, 27, 28, 29]) formulations to overcome this drawback. In the IRBF-based methods, the integration process generates some unknown integration constants. This provides effective ways to add some extra information through the process of converting the RBF weights into the function values to improve the solution accuracy. For example, through integration constants, one can impose derivative boundary conditions at the two end points of a grid line in an exact manner. Mai-Duy and Tran-Cong [28] proposed a compact five-point stencil based on IRBF networks for solving 2D second-order differential problems. In this compact IRBF stencil, not only the nodal function values but also the nodal derivative values are incorporated into the IRBF approximations.

The rational function transformation (RFT) method was proposed by Pan and Wierenga [3, 4] in combination with FDM to solve the Richards equation. Their numerical results showed that the RFT method with a modified Picard method are more efficient than the h-based modified Picard method [1] and the φ-based transformation method [2] in handling the nonlinearity of the Richards equation. In the present paper, we develop a numerical procedure based on the compact integrated radial basis function (CIRBF) scheme (instead of the conventional FDM) for the spatial discretisation in combination with the RFT method to accurately simulate moisture motion in heterogeneous soils. The present approach is a generalised finite difference (GDF) scheme since the spatial derivatives are discretised in terms of the information of neighbouring nodes and then substituted into the strong form of the governing equations to obtain a system of algebraic

3

equations [15, 16, 17, 18, 19]. Before solving the soil problems, we verify the CIRBF scheme by solving some 2–D Poisson equations and a nonlinear fluid flow problem (i.e., Taylor-Green vortex).

The paper is organised as follows. Section 2 presents the CIRBF scheme, followed by a discussion of the governing equations for moisture motion in soils in Section 3. In Section 4 the CIRBF scheme is verified. The proposed method is then applied to solve 1–D and 2–D soil infiltration problems in Section 5. Section 6 concludes the paper.

2. Compact integrated radial basis function technique

In this section, we use the notation

- $\bar{[\ ]}$ for a vector/matrix $[\ ]$ that is associated with a CIRBF stencil;

- $\widehat{[\ ]}$ for a vector/matrix $[\ ]$ that is associated with a grid line;

- $[\ ]_{(\eta,\theta)}$ to denote selected rows η and columns θ of the matrix $[\ ]$;

- $[\ ]_{(\eta)}$ to denote selected components η of the vector $[\ ]$;

- $[\ ]_{(:,\theta)}$ to denote all rows and selected columns θ of the matrix $[\ ]$; and

- $[\ ]_{(\eta,:)}$ to denote all columns and selected rows η of the matrix $[\ ]$.

Consider a CIRBF stencil associated with three nodal points $\{i-1, i, i+1\}$ on an x–grid line with n nodal points as shown in Fig. 1. An approximation of the field variable u at a nodal point x_i is sought in the form

$$\frac{\partial^2 u(x)}{\partial x^2} = \sum_{k=i-1}^{k=i+1} w^{(k)} G^{(k)}(x), \tag{2.1}$$

$$\frac{\partial u(x)}{\partial x} = \sum_{k=i-1}^{k=i+1} w^{(k)} H_{[1]}^{(k)}(x) + c_1, \tag{2.2}$$

$$u(x) = \sum_{k=i-1}^{k=i+1} w^{(k)} H_{[0]}^{(k)}(x) + c_1 x + c_2, \tag{2.3}$$

where $\left\{ w^{(k)} \right\}_{k=i-1}^{k=i+1}$ are RBF weights to be determined; $G^{(k)}(x)$ known RBFs; $H_{[1]}(x) = \int G(x)dx$; $H_{[0]}(x) = \int H_{[1]}(x)dx$; and c_1 and c_2 integration constants which are also unknown. An example of RBF, used in this work, is the

multiquadrics $G^{(k)}(x) = \sqrt{(x - x^{(k)})^2 + a^{(k)2}}$, where $a^{(k)}$ is the RBF width determined presently as $a^{(k)} = \beta' g$, in which β' is a positive factor, and g the grid size. The large values of β' lead to RBFs with a flat shape that yield more accurate results but also produce an ill-conditioned interpolation matrix. Therefore, it is important to find the appropriate values of β'. So far the RBF width has been chosen either by empirical approaches or by optimization techniques [30, 31].

For the compact IRBF approximation of the first- and second-order derivatives, the nodal function values and extra information are included to establish the stencil approximation. In the CIRBF scheme presented in [32], nodal first-derivatives are chosen as extra information in the compact approximation of first derivatives while nodal second-derivatives are used in the compact approximation of second derivatives. In the present CIRBF scheme, the information of nodal second derivatives are employed in both the compact approximations of first and second derivatives as described in the following sub-sections. The performance of both methods are compared through a numerical example in Section 4.3. The nodal function values and the nodal second derivatives (extra information) are used to establish the relation between the physical space and the RBF weight space. Application of (2.3) at three nodal points $\{i - 1, i, i + 1\}$ and (2.1) at two nodal points $\{i - 1, i + 1\}$ results in

$$
\begin{pmatrix} \bar{u} \\ \frac{\partial^2 u^{(i-1)}}{\partial x^2} \\ \frac{\partial^2 u^{(i+1)}}{\partial x^2} \end{pmatrix} = \underbrace{\begin{bmatrix} H_{[0]}^{(i-1)}(x_{i-1}) & H_{[0]}^{(i)}(x_{i-1}) & H_{[0]}^{(i+1)}(x_{i-1}) & x_{i-1} & 1 \\ H_{[0]}^{(i-1)}(x_i) & H_{[0]}^{(i)}(x_i) & H_{[0]}^{(i+1)}(x_i) & x_i & 1 \\ H_{[0]}^{(i-1)}(x_{i+1}) & H_{[0]}^{(i)}(x_{i+1}) & H_{[0]}^{(i)}(x_{i+1}) & x_{i+1} & 1 \\ G^{(i-1)}(x_{i-1}) & G^{(i)}(x_{i-1}) & G^{(i+1)}(x_{i-1}) & 0 & 0 \\ G^{(i-1)}(x_{i+1}) & G^{(i)}(x_{i+1}) & G^{(i)}(x_{i+1}) & 0 & 0 \end{bmatrix}}_{\mathbf{C}} \begin{pmatrix} \bar{w} \\ \bar{c} \end{pmatrix}
$$

$$(2.4)$$

or

$$
\begin{pmatrix} \bar{w} \\ \bar{c} \end{pmatrix} = \mathbf{C}^{-1} \begin{pmatrix} \bar{u} & \frac{\partial^2 u^{(i-1)}}{\partial x^2} & \frac{\partial^2 u^{(i+1)}}{\partial x^2} \end{pmatrix}^T
$$

$$(2.5)$$

in which $\bar{u} = \begin{pmatrix} u^{(i-1)} & u^{(i)} & u^{(i+1)} \end{pmatrix}^T$; $\bar{w} = \begin{pmatrix} w^{(i-1)} & w^{(i)} & w^{(i+1)} \end{pmatrix}^T$; and $\bar{c} = \begin{pmatrix} c_1 & c_2 \end{pmatrix}^T$. In the following sub-sections, the relation (2.5) is used in combination with Eqs. (2.1) and (2.2) to find the expression of first and second derivatives of the field variable u in the physical space.

2.1. CIRBF approximation of second derivative

The second derivative of the field variable u at a nodal point x_i is calculated based on Eq. (2.1) as

$$\frac{\partial^2 u^{(i)}}{\partial x^2} = G^{(i-1)}(x_i)w^{(i-1)} + G^{(i)}(x_i)w^{(i)} + G^{(i+1)}(x_i)w^{(i+1)} \qquad (2.6)$$

or

$$\frac{\partial^2 u^{(i)}}{\partial x^2} = \begin{bmatrix} G^{(i-1)}(x_i) & G^{(i)}(x_i) & G^{(i+1)}(x_i) & 0 & 0 \end{bmatrix} \begin{pmatrix} w^{(i-1)} & w^{(i)} & w^{(i+1)} & c_1 & c_2 \end{pmatrix}^T$$
$$(2.7)$$

or

$$\frac{\partial^2 u^{(i)}}{\partial x^2} = \mathbf{G}(x_i) \begin{pmatrix} \bar{w} & \bar{c} \end{pmatrix}^T. \qquad (2.8)$$

Substituting (2.5) into (2.8) results in

$$\frac{\partial^2 u^{(i)}}{\partial x^2} = \underbrace{\mathbf{G}(x_i)\mathbf{C}^{-1}}_{\mathbf{R}_2} \begin{pmatrix} \bar{u} & \frac{\partial^2 u^{(i-1)}}{\partial x^2} & \frac{\partial^2 u^{(i+1)}}{\partial x^2} \end{pmatrix}^T \qquad (2.9)$$

or

$$\frac{\partial^2 u^{(i)}}{\partial x^2} = \mathbf{R}_{2a}\bar{u} + \mathbf{R}_{2b} \begin{pmatrix} \frac{\partial^2 u^{(i-1)}}{\partial x^2} & \frac{\partial^2 u^{(i+1)}}{\partial x^2} \end{pmatrix}^T \qquad (2.10)$$

where $\mathbf{G}(x_i)$ is a known matrix of dimension 1×5; $\mathbf{R}_{2a} = \mathbf{R}_2(1:3)$ and $\mathbf{R}_{2b} = \mathbf{R}_2(4:5)$. Eq. (2.10) can be expressed as

$$\mathbf{L}\frac{\partial^2 \bar{u}}{\partial x^2} = \mathbf{R}_{2a}\bar{u} \qquad (2.11)$$

in which $\mathbf{L}$ is a known matrix of dimension 1×3.

To calculate function derivatives at the boundary nodes 1 and n, we use CIRBF stencils consisting of four nodes as shown in Fig. 1b. We use the same approach as presented in [29, 32] for boundary condition treatments. Note that the boundary stencils have more nodes than the interior stencils and according to numerical experiments this treatment yields the most accurate solution. Application of (2.3) at four nodal points $\{1, 2, 3, 4\}$ and (2.1) at the nodal point 2 results in

6

$$
\begin{pmatrix}
u^{(1)} \\
u^{(2)} \\
u^{(3)} \\
u^{(4)} \\
\frac{\partial^2 u^{(2)}}{\partial x^2}
\end{pmatrix}
=
\underbrace{
\begin{bmatrix}
H_{[0]}^{(1)}(x_1) & H_{[0]}^{(2)}(x_1) & H_{[0]}^{(3)}(x_1) & H_{[0]}^{(4)}(x_1) & x_1 & 1 \\
H_{[0]}^{(1)}(x_2) & H_{[0]}^{(2)}(x_2) & H_{[0]}^{(3)}(x_2) & H_{[0]}^{(4)}(x_2) & x_2 & 1 \\
H_{[0]}^{(1)}(x_3) & H_{[0]}^{(2)}(x_3) & H_{[0]}^{(3)}(x_3) & H_{[0]}^{(4)}(x_3) & x_3 & 1 \\
H_{[0]}^{(1)}(x_4) & H_{[0]}^{(2)}(x_4) & H_{[0]}^{(3)}(x_4) & H_{[0]}^{(4)}(x_4) & x_4 & 1 \\
G^{(1)}(x_2) & G^{(2)}(x_2) & G^{(3)}(x_2) & G^{(4)}(x_2) & 0 & 0
\end{bmatrix}
}_{\mathbf{C}'}
\begin{pmatrix}
w^{(1)} \\
w^{(2)} \\
w^{(3)} \\
w^{(4)} \\
\bar{c}
\end{pmatrix}
$$

$$(2.12)$$

or

$$
\left(w^{(1)} \ w^{(2)} \ w^{(3)} \ w^{(4)} \ \bar{c} \right)^T = \mathbf{C}'^{-1} \left(u^{(1)} \ u^{(2)} \ u^{(3)} \ u^{(4)} \ \frac{\partial^2 u^{(2)}}{\partial x^2} \right)^T, \qquad (2.13)
$$

in which the matrix $\mathbf{C}'$ is underdetermined and its inverse can be found using the singular value decomposition technique.

Substituting (2.13) into (2.1) and applying at a nodal point 1 result in

$$
\frac{\partial^2 u^{(1)}}{\partial x^2} = \underbrace{\mathbf{G}(x_1)\mathbf{C}'^{-1}}_{\mathbf{R}'_2} \left(u^{(1)} \ u^{(2)} \ u^{(3)} \ u^{(4)} \ \frac{\partial^2 u^{(2)}}{\partial x^2} \right)^T \qquad (2.14)
$$

or

$$
\frac{\partial^2 u^{(1)}}{\partial x^2} = \mathbf{R}'_{2a} \left(u^{(1)} \ u^{(2)} \ u^{(3)} \ u^{(4)} \right)^T + \mathbf{R}'_{2b} \left(\frac{\partial^2 u^{(2)}}{\partial x^2} \right) \qquad (2.15)
$$

where $\mathbf{G}(x_1)$ is a known matrix of dimension 1×6; $\mathbf{R}'_{2a} = \mathbf{R}'_2(1:4)$ and $\mathbf{R}'_{2b} = \mathbf{R}'_2(5)$. Eq. (2.15) can be expressed as

$$
\mathbf{L}' \left(\frac{\partial^2 u^{(1)}}{\partial x^2} \ \frac{\partial^2 u^{(2)}}{\partial x^2} \right)^T = \mathbf{R}'_{2a} \left(u^{(1)} \ u^{(2)} \ u^{(3)} \ u^{(4)} \right)^T \qquad (2.16)
$$

in which $\mathbf{L}'$ is a known matrix of dimension 1×2. Similarly, the CIRBF stencil associated with the boundary node n is constructed as

$$
\mathbf{L}'' \left(\frac{\partial^2 u^{(n-1)}}{\partial x^2} \ \frac{\partial^2 u^{(n)}}{\partial x^2} \right)^T = \mathbf{R}''_{2a} \left(u^{(n-3)} \ u^{(n-2)} \ u^{(n-1)} \ u^{(n)} \right)^T \qquad (2.17)
$$

in which $\mathbf{L}''$ and $\mathbf{R}''_{2a}$ are known matrices of dimensions 1×2 and 1×4, respectively.

7

From Eqs. (2.11), (2.16) and (2.17), the value of second-derivative of u w.r.t. x at nodal points on the $x-$ grid line is given by

$$\hat{\mathbf{L}}\frac{\partial^2 \hat{u}}{\partial x^2} = \hat{\mathbf{R}}_{2a}\hat{u} \tag{2.18}$$

or

$$\frac{\partial^2 \hat{u}}{\partial x^2} = \hat{\mathbf{D}}_{2x}\hat{u} \tag{2.19}$$

where $\hat{u} = \{u^{(1)} \ u^{(2)} \ ... \ u^{(n)}\}^T$; $\hat{\mathbf{L}}$ and $\hat{\mathbf{R}}_{2a}$ are known matrices of dimensions $n \times n$ (n is defined earlier in the text just above Eq. (2.1) and in Fig. 1); and $\hat{\mathbf{D}}_{2x} = \hat{\mathbf{L}}^{-1}\hat{\mathbf{R}}_{2a}$.

2.2. CIRBF approximation of first derivative

The first derivative of the field variable u at a nodal point x_i is calculated based on Eq. (2.2) as

$$\frac{\partial u^{(i)}}{\partial x} = H^{(i-1)}_{[1]}(x_i)w^{(i-1)} + H^{(i)}_{[1]}(x_i)w^{(i)} + H^{(i+1)}_{[1]}(x_i)w^{(i+1)} + c_1 \tag{2.20}$$

or

$$\frac{\partial u^{(i)}}{\partial x} = \left[\begin{array}{ccccc} H^{(i-1)}_{[1]}(x_i) & H^{(i)}_{[1]}(x_i) & H^{(i+1)}_{[1]}(x_i) & 1 & 0 \end{array} \right] \left(\begin{array}{ccccc} w^{(i-1)} & w^{(i)} & w^{(i+1)} & c_1 & c_2 \end{array} \right)^T \tag{2.21}$$

or

$$\frac{\partial u^{(i)}}{\partial x} = \mathbf{H}_{[1]}(x_i) \left(\begin{array}{cc} \bar{w} & \bar{c} \end{array} \right)^T. \tag{2.22}$$

Substituting (2.5) into (2.22) results in

$$\frac{\partial u^{(i)}}{\partial x} = \underbrace{\mathbf{H}_{[1]}(x_i)\mathbf{C}^{-1}}_{\mathbf{R}_1} \left(\begin{array}{ccc} \bar{u} & \frac{\partial^2 u^{(i-1)}}{\partial x^2} & \frac{\partial^2 u^{(i+1)}}{\partial x^2} \end{array} \right)^T \tag{2.23}$$

or

$$\frac{\partial u^{(i)}}{\partial x} = \mathbf{R}_{1a}\bar{u} + \mathbf{R}_{1b} \left(\begin{array}{cc} \frac{\partial^2 u^{(i-1)}}{\partial x^2} & \frac{\partial^2 u^{(i+1)}}{\partial x^2} \end{array} \right)^T \tag{2.24}$$

where $\mathbf{H}_{[1]}(x_i)$ is a known matrix of dimension 1×5; $\mathbf{R}_{1a} = \mathbf{R}_1(1:3)$ and $\mathbf{R}_{1b} = \mathbf{R}_1(4:5)$. Making use of (2.19), Eq. (2.24) becomes

$$\frac{\partial u^{(i)}}{\partial x} = \mathbf{R}_{1a}\bar{u} + \mathbf{R}_{1b}\hat{\mathbf{D}}_{2x}(idi', :)\hat{u} \tag{2.25}$$

8

where idi' is the index vector mapping the location of nodes $\{i-1, i+1\}$ to that in the $x-$ grid line.

For the boundary node 1, substituting (2.13) into (2.2) and applying at the nodal points 1 result in

$$\frac{\partial u^{(1)}}{\partial x} = \underbrace{\mathbf{H}_{[1]}(x_1)\mathbf{C}'^{-1}}_{\mathbf{R}'_1}\left(u^{(1)}\ u^{(2)}\ u^{(3)}\ u^{(4)}\ \frac{\partial^2 u^{(2)}}{\partial x^2}\right)^T \qquad (2.26)$$

or

$$\frac{\partial u^{(1)}}{\partial x} = \mathbf{R}'_{1a}\left(u^{(1)}\ u^{(2)}\ u^{(3)}\ u^{(4)}\right)^T + \mathbf{R}'_{1b}\left(\frac{\partial^2 u^{(2)}}{\partial x^2}\right) \qquad (2.27)$$

where $\mathbf{H}_{[1]}(x_1)$ is a known matrix of dimension 1×6; $\mathbf{R}'_{1a} = \mathbf{R}'_1(1:4)$ and $\mathbf{R}'_{1b} = \mathbf{R}'_1(5)$. Making use of (2.19), Eq. (2.27) becomes

$$\frac{\partial u^{(1)}}{\partial x} = \mathbf{R}'_{1a}\left(u^{(1)}\ u^{(2)}\ u^{(3)}\ u^{(4)}\right)^T + \mathbf{R}'_{1b}\hat{\mathbf{D}}_{2x}(2,:)\hat{u}. \qquad (2.28)$$

The value of the first-order derivative of u w.r.t. x at the nodal point n is determined in the similar manner as

$$\frac{\partial u^{(n)}}{\partial x} = \mathbf{R}''_{1a}\left(u^{(n-3)}\ u^{(n-2)}\ u^{(n-1)}\ u^{(n)}\right)^T + \mathbf{R}''_{1b}\hat{\mathbf{D}}_{2x}(n-1,:)\hat{u} \qquad (2.29)$$

where $\mathbf{R}''_{1a}$ and $\mathbf{R}''_{1b}$ are known matrices of dimensions 1×4 and 1×1, respectively.

From Eqs. (2.25), (2.28) and (2.29), the value of first-derivative of u w.r.t. x at nodal points on the $x-$ grid line is given by

$$\frac{\partial \hat{u}}{\partial x} = \hat{\mathbf{D}}_{1x}\hat{u} \qquad (2.30)$$

in which $\hat{\mathbf{D}}_{1x}$ is a known matrix of dimension $n \times n$.

Similarly, the values of the second-order and first-order derivatives of u w.r.t. y at nodal points on a $y-$ grid line is given by

$$\frac{\partial^2 \hat{u}}{\partial y^2} = \hat{\mathbf{D}}_{2y}\hat{u}, \qquad (2.31)$$

$$\frac{\partial \hat{u}}{\partial y} = \hat{\mathbf{D}}_{1y}\hat{u}. \qquad (2.32)$$

For both rectangular and non-rectangular domain problems, the boundary conditions can be imposed in a straightforward manner via a boundary stencil such as one described by Eq. (2.12). Additionally, problems having strong boundary layer effects, e.g. lid-driven cavity flows and natural convection flows, can be solved at a high level of accuracy owing to the use of the IRBFs to construct the local approximations as reported in the previous published works by Mai-Duy and Tran-Cong [28], Thai-Quang et al. [29] and Ngo-Cong et al. [33].

3. Governing equation for moisture motion in soil

Moisture motion in soils obeys the Richards equation which can be written in three forms as follows [1].

- The "h-based" form

$$C(h)\frac{\partial h}{\partial t} - \nabla\left(K(h)\nabla h\right) - \frac{\partial K}{\partial z} = 0 \qquad (3.33)$$

- The "θ-based" form

$$\frac{\partial \theta}{\partial t} - \nabla\left(D(\theta)\nabla\theta\right) - \frac{\partial K}{\partial z} = 0 \qquad (3.34)$$

- The "mixed form"

$$\frac{\partial \theta}{\partial t} - \nabla\left(K(h)\nabla h\right) - \frac{\partial K}{\partial z} = 0 \qquad (3.35)$$

where h is pressure head measured in the length unit $[L]$; θ the moisture content $[L^3/L^3]$; $C(h) = d\theta/dh$ the specific moisture capacity function $[1/L]$; $K(h)$ is the unsaturated hydraulic conductivity $[L/T]$; $D(\theta) = K(\theta)/C(\theta)$ the unsaturated diffusivity $[L^2/T]$, z denotes the vertical dimension $[L]$, assumed positive upward.

As discussed in Celia et al. [1], numerical solutions based on the standard h-based form generally yield poor results due to large mass balance errors. In contrast, numerical solutions based on the mixed form possess the conservative property, resulting in mass conservation and more accurate numerical solution. The "mixed" form (3.35) was discretised by Celia et al. [1] as follows.

$$\frac{C^{(n_t+1,m)}}{\Delta t}\delta^m - \nabla\cdot\left(K^{(n_t+1,m)}\nabla\delta^m\right) = \\ \nabla\cdot\left(K^{(n_t+1,m)}\nabla h^{(n_t+1,m)}\right) + \frac{\partial K^{(n_t+1,m)}}{\partial z} + \frac{\theta^{(n_t)}-\theta^{(n_t+1,m)}}{\Delta t}, \qquad (3.36)$$

10

or

$$\frac{C^{(n_t+1,m)}}{\Delta t}\delta - \frac{\partial}{\partial x}\left(K^{(n_t+1,m)}\frac{\partial \delta}{\partial x}\right) - \frac{\partial}{\partial z}\left(K^{(n_t+1,m)}\frac{\partial \delta}{\partial z}\right) =$$
$$\frac{\partial}{\partial x}\left(K^{(n_t+1,m)}\frac{\partial h^{(n_t+1,n)}}{\partial x}\right) + \frac{\partial}{\partial z}\left(K^{(n_t+1,m)}\frac{\partial h^{(n_t+1,n)}}{\partial z}\right) + \frac{\partial K^{(n_t+1)}}{\partial z} + \frac{\theta^{(n_t)}-\theta^{(n_t+1,m)}}{\Delta t}$$

(3.37)

where $\delta^m = h^{(n_t+1,m+1)} - h^{(n_t+1,m)}$; the superscript (n_t) refers to a time level; and (m) a pseudo-time level (Picard iterations).

In the present study we discretise the "mixed" form based on the rational function transformation (RFT) method proposed by Pan and Wierenga [3]. In the RFT method, a transform function f is designed as follows.

$$f = \begin{cases} \frac{h}{1+\beta h} & if \ h < 0 \\ h & if \ h \geq 0 \end{cases}$$

(3.38)

or

$$h = \begin{cases} \frac{f}{1-\beta f} & if \ h < 0 \\ f & if \ h \geq 0 \end{cases}$$

(3.39)

$$\Rightarrow \frac{\partial h}{\partial f} = \begin{cases} (1+\beta h)^2 & if \ h < 0 \\ 1 & if \ h \geq 0 \end{cases}$$

(3.40)

where β is a transform constant. Making use of (3.39) and (3.40), (3.35) becomes

$$\frac{\partial \theta}{\partial t} - \nabla\left(K^*\nabla f\right) - \frac{\partial K}{\partial z} = 0$$

(3.41)

The time discretisation for (3.41) is also carried out using the modified Picard method of Celia et al. [1] as follows.

$$\frac{C^*\delta f}{\Delta t} - \frac{\partial}{\partial x}\left(K^*\frac{\partial \delta f}{\partial x}\right) - \frac{\partial}{\partial z}\left(K^*\frac{\partial \delta f}{\partial z}\right) =$$
$$-\frac{\partial q_x^{(n_t+1,m)}}{\partial x} - \frac{\partial q_z^{(n_t+1,m)}}{\partial z} + \frac{\theta^{(n_t)}-\theta^{(n_t+1,m)}}{\Delta t}$$

(3.42)

where $\delta f^m = f^{(n_t+1,m+1)} - f^{(n_t+1,m)}$; $q_x = -K^*\partial f/\partial x$, $q_z = -K^*\partial f/\partial z - K$, $C^* = C\partial h/\partial f$ and $K^* = K\partial h/\partial f$. In each physical time step, the convergence is achieved during the modified Picard iterations if the values of f satisfy the following convergence criterion.

$$\frac{\sqrt{\sum_{i=1}^{N}\left(f_i^{(m+1)} - f_i^{(m)}\right)^2}}{\sqrt{\sum_{i=1}^{N}\left(f_i^{(m+1)}\right)^2}} < TOL,$$

(3.43)

11

where TOL is a given tolerance and presently set to be 10^{-5}.

Pan and Wierenga [3] suggested to choose the value of β as big as possible as long as the K^* versus f curves are still monotonic and recommended $\beta = -0.04cm^{-1}$ as the universal value. In the present study, we use this value of β. The spatial discretisation for (3.42) is carried out by using the CIRBF scheme by replacing the function u in Section 2 by the functions f and δf.

4. Verification of the CIRBF scheme

Before applying the present CIRBF scheme to simulate flow motion in soils, we verify the method through the solution of a 2–D Poisson equation and a Taylor-Green vortex. We evaluate the performance of the present scheme based on the root mean square error (RMS), the relative L_2 error (Ne) and the convergence rate ($O(g^{\alpha'})$).

$$RMS = \sqrt{\frac{\sum_{i=1}^{N} (u_i - \overline{u}_i)^2}{N}}, \tag{4.44}$$

$$RMS(g) \approx \gamma' g^{\alpha'} = O(g^{\alpha'}), \tag{4.45}$$

$$Ne = \sqrt{\frac{\sum_{i=1}^{N} (u_i - \overline{u}_i)^2}{\sum_{i=1}^{N} \overline{u}_i^2}}, \tag{4.46}$$

$$Ne(g) \approx \gamma' g^{\alpha'} = O(g^{\alpha'}), \tag{4.47}$$

where u_i and $\overline{u}_i$ are the numerical and exact solutions at the i-th node, respectively; and N the number of nodes over the whole domain; and γ' and α' are exponential model's parameters. For the purpose of computational cost comparisons, all related computations are carried out on a Dell computer with an Intel Core (TM) i7-3770, 3.40 GHz processor, 8 GB RAM and 64-bit operating system.

4.1. Ordinary differential equations (ODEs)

In this sub-section, we study the performance of the present approach over uniform and non-uniform distributions of collocation points through the solution of two ODEs. The first one (ODE-1) is

$$\frac{d^2u}{dx^2} = -16\pi^2 \sin\left(4\pi x\right), \, 0 \le x \le 1 \tag{4.48}$$

12

subject to the Dirichlet boundary condition derived from the exact solution $\bar{u} = 3 + \sin(4\pi x)$. The second one (ODE-2) has a more complicated form,

$$\frac{d^2 u}{dx^2} - 3\frac{du}{dx} + 2u = \exp(4x), \ -1 \leq x \leq 1 \tag{4.49}$$

subject to the Dirichlet boundary condition derived from the exact solution $\bar{u} = 2\exp(x) + \exp(2x) + (1/6)\exp(4x)$.

Over $0 \leq x \leq 1$ we determine the distribution of collocation points $x = \{x_i\}_{i=1}^N$ through the relation

$$x_{i+1} = x_i + g_i, \ 1 \leq i \leq N - 1, \tag{4.50}$$

where $x_1 = 0$, $g_i = g_0/\rho_i$, $g_0 = 1/(N-1)$ and ρ is a density function which is presently chosen as

$$\rho(i) = \exp\left(a_\rho \frac{i}{N}\right), \ i = 1, 2, ..., N, \tag{4.51}$$

in which a_ρ is positive and the larger the value of a_ρ the more non-uniform the distribution of collocation point will be. The distribution is then normalised so that $0 \leq x \leq 1$. We take a mirror image for $-1 \leq x \leq 0$.

The ODEs are solved on a set of uniform ($a_\rho = 0$) and non-uniform ($a_\rho = \{0.5, 1.0, 1.5\}$) grids with different sizes $N = \{101, 201, ..., 1001\}$. For ODE-1, its solution accuracy (Ne) against the RBF width (β') is presented in Fig. 2 (for $N = 501$) while the behaviour of Ne against the number of grid nodes is presented in Fig. 3 (for $\beta' = 50$). The corresponding results for ODE-2 are given in Figs. 4 and 5. The four figures show that the present approach yields greater accuracy for uniform grids ($a_\rho = 0$) and the accuracy increases as a_ρ is reduced. We will use uniform grids for the following computations.

4.2. Poisson equation

4.2.1. Poisson equation in a square domain:

In order to study the spatial accuracy of the present CIRBF approximation scheme, we consider the following Poisson equation

$$\frac{\partial^2 u}{\partial x^2} + \frac{\partial^2 u}{\partial y^2} = -18\pi^2 \sin(3\pi x)\sin(3\pi y), \tag{4.52}$$

subject to the Dirichlet boundary condition derived from the following exact solution

$$\bar{u} = \sin(3\pi x)\sin(3\pi y) \tag{4.53}$$

in which $0 \leq x, y \leq 1$. The calculations are carried out on a set of uniform grids of $\{21 \times 21, 31 \times 31, ..., 71 \times 71\}$. Table 1 gives comparison of numerical solutions showing that the proposed scheme outperforms the higher order compact finite difference (HOC) scheme [34], 1D-IRBF [12] and finite difference method with central-difference (FDM) scheme. The convergence rate is $O(g^{2.036})$ for the FDM scheme, $O(g^{3.052})$ for the 1D-IRBF scheme, $O(g^{4.837})$ for the HOC scheme, and $O(g^{4.847})$ for the present scheme.

To compare the computational cost of the CIRBF, 1D-IRBF and HOC schemes, we let the grid size increase as $\{21 \times 21, 22 \times 22, ...\}$ until the solution accuracy achieves a target RMS level of 10^{-5}. Fig. 6 shows that the present scheme takes much less time to reach the target accuracy than the 1D-IRBF and the HOC. It is noted that the final grid size used to achieve the target accuracy is 81×81 for the 1D-IRBF, 45×45 for the HOC, and 44×44 for the present CIRBF. Fig. 7 presents the RMS of the approximate solution u against the RBF width parameter β' for three different grids $(31 \times 31, 51 \times 51$ and $71 \times 71)$. The solution accuracy becomes better as β' increases to a certain value ($\beta' = 10$ for the 31×31 grid, $\beta' = 20$ for the 51×51 grid, and $\beta' = 30$ for the 71×71 grid) and beyond that the accuracy is almost unchanged.

4.2.2. Poisson equation in a square domain with a circular hole:

The present method is also verified through the solution of the following 2D Poisson equation

$$\frac{\partial^2 u}{\partial x^2} + \frac{\partial^2 u}{\partial y^2} = -8\pi^2 \sin(2\pi x) \sin(2\pi y), \qquad (4.54)$$

defined on a non-rectangular domain as shown in Fig. 8 and subject to Dirichlet boundary conditions. The problem has the following exact solution

$$\overline{u} = \sin(2\pi x) \sin(2\pi y), \qquad (4.55)$$

from which the boundary values of u can be derived.

Fig. 9 presents the grid convergence study for the present CIRBF method in comparison with that of the 1D-IRBF and MLS-1D-IRBF methods [26]. The numerical results show that the present method yields more accurate solutions than its counterparts and has a higher convergence rate (error norm of $O(g^{4.12})$) than the 1D-IRBF (error norm of $O(g^{3.00})$) and the MLS-1D-IRBF (error norm of $O(g^{3.70})$). Fig. 10 presents the relative L_2 errors (Ne)

14

of the approximate solution u against the RBF width parameter β' for three different grids. It can be seen that the optimal value of β' varies with different grids (i.e., $\beta' = 3$ for the 25×25 grid, $\beta' = 6$ for the 49×49 grid, and $\beta' = 10$ for the 73×73 grid). And, for a given grid size, the solution accuracy is almost unchanged with large values of β'. When solving arbitrary problems which do not have analytical solutions, it could be difficult to determine the optimal RBF width. In those problems, we suggest to choose β' large enough (e.g., $\beta' = 15$) to obtain stable and accurate numerical results.

4.3. Taylor-Green vortex

The Taylor-Green vortex is modelled by the incompressible transient Navier-Stokes equations written in the dimensionless non-conservative forms as

$$\frac{\partial u}{\partial x} + \frac{\partial v}{\partial y} = 0, \tag{4.56}$$

$$\frac{\partial u}{\partial t} + u\frac{\partial u}{\partial x} + v\frac{\partial u}{\partial y} = -\frac{\partial p}{\partial x} + \frac{1}{\mathrm{Re}}\left(\frac{\partial^2 u}{\partial x^2} + \frac{\partial^2 u}{\partial y^2}\right), \tag{4.57}$$

$$\frac{\partial v}{\partial t} + u\frac{\partial v}{\partial x} + v\frac{\partial v}{\partial y} = -\frac{\partial p}{\partial y} + \frac{1}{\mathrm{Re}}\left(\frac{\partial^2 v}{\partial x^2} + \frac{\partial^2 v}{\partial y^2}\right), \tag{4.58}$$

where u, v and p are velocity components in x-, y-direction and static pressure, respectively; $\mathrm{Re} = Ul/\nu$ the Reynolds number, in which ν, l and U are the kinematic viscosity, characteristic length and characteristic speed of the flow, respectively. Consider Eqs. (4.56)–(4.58) with the initial condition

$$\overline{u}(x, y) = -\cos(\kappa x)\sin(\kappa y), \tag{4.59}$$

$$\overline{v}(x, y) = \sin(\kappa x)\cos(\kappa y), \tag{4.60}$$

where $0 \leq x, y \leq 2\pi$ and $\kappa = 2$. The analytic solution for this problem is

$$\overline{u}(x, y, t) = -\cos(\kappa x)\sin(\kappa y)\exp(-2\kappa^2 t/\mathrm{Re}), \tag{4.61}$$

$$\overline{v}(x, y, t) = \sin(\kappa x)\cos(\kappa y)\exp(-2\kappa^2 t/\mathrm{Re}), \tag{4.62}$$

$$\overline{p}(x, y, t) = -1/4\left\{\cos(2\kappa x) + \cos(2\kappa y)\right\}\exp(-4\kappa^2 t/\mathrm{Re}). \tag{4.63}$$

The boundary conditions for u, v and p can be derived from (4.61)–(4.63).

The CIRBF scheme which is incorporated into the fully coupled approach where velocities and pressure are concurrently solved [32, 35, 36], called as

15

CIRBF-Fully Coupled, is applied to solve this problem at $Re = 100$. A time step is taken to be $\Delta t = 0.002$. The present numerical results are compared with those obtained by Tian et al. [34] who used the upwind HOC scheme based on a fractional step approach and a staggered grid system (HOC-Fractional). For the purpose of comparison, we also implement the HOC scheme [34] into the present fully coupled fluid solver, named as HOC-Fully Coupled. Table 2 shows the accuracy comparison between the CIRBF-Fully Coupled, HOC-Fully Coupled and HOC-Fractional at time $t = 2$ for different grid sizes. It is seen that CIRBF-Fully Coupled approach yields much better accuracy and better convergence rates than the HOC-Fractional [34], and also performs better than the HOC-Fully Coupled. To investigate the computational efficiency of the CIRBF and HOC schemes when solving the time-dependent problem, we increase the grid size as $\{11 \times 11, 13 \times 13, ...\}$ until the solution accuracy of the u-velocity achieves a target RMS level of 10^{-3}. Fig. 11 shows that the present-CIRBF scheme reaches the target accuracy faster than the HOC approach. It is noted that the final grid size used to achieve the target accuracy is 29×29 for the HOC, 29×29 for the previous CIRBF, and 27×27 for the present CIRBF. We also compare the present CIRBF results with those of the previous CIRBF scheme presented by Tien et al. [32]. The numerical results show that the present scheme performs better than the previous scheme as shown in Fig. 11.

5. Numerical results and discussion

In this section, we apply the proposed numerical approach based on the CIRBF scheme and the rational function transformation (RFT) method to simulate 1–D moisture motions in homogeneous and layered soils and 2–D moisture motions in heterogeneous soils.

5.1. One-dimensional flow in a homogeneous soil

The performance of the proposed numerical approach is investigated through three different sets of soil properties as follows.

- Set 1: The soil property is modelled as [37]

$$\theta(h) = \frac{\hat{\alpha} \left(\theta_s - \theta_r \right)}{\hat{\alpha} + |h|^{\hat{\beta}}} + \theta_r, \tag{5.64}$$

$$K(h) = K_s \frac{A}{A + |h|^{\gamma}}, \tag{5.65}$$

16

where $\hat{\alpha} = 1.611 \times 10^6$, $\theta_s = 0.287$, $\theta_r = 0.075$, $\hat{\beta} = 3.96$, $K_s = 0.00944cm/s$, $A = 1.175 \times 10^6$ and $\gamma = 4.74$. Initial and boundary conditions are $h(z, t = 0) = -61.5cm$, $h_{top} = h(40cm, t) = -20.7cm$, and $h_{bottom} = h(0, t) = -61.5cm$ (Fig. 12).

- Set 2: The soil property is modelled as [1]

$$\theta(h) = \frac{\theta_s - \theta_r}{[1 + (\alpha\,|h|)^\eta]^\mu} + \theta_r, \tag{5.66}$$

$$K(h) = K_s \frac{\left\{1 - (\alpha\,|h|)^{\eta-1}\,[1 + (\alpha\,|h|)^\eta]^{-\mu}\right\}^2}{[1 + (\alpha\,|h|)^\eta]^{\mu/2}}, \tag{5.67}$$

where $\alpha = 0.0335$, $\theta_s = 0.368$, $\theta_r = 0.102$, $\eta = 2, \mu = 0.5$, $K_s = 0.00922cm/s$. Initial and boundary conditions are $h(z, t = 0) = -1000cm$, $h_{top} = h(100cm, t) = -75cm$, and $h_{bottom} = h(0, t) = -1000cm$.

- Set 3: The Mualen-van Genuchten (MG) model is used as [38, 8]

$$\theta = \begin{cases} \frac{\theta_s - \theta_r}{[1+(\alpha|h|)^\eta]^\mu} + \theta_r & \text{if } h \leq 0 \\ \theta_s & \text{if } h > 0 \end{cases} \tag{5.68}$$

$$K = \begin{cases} K_s S_e^{\hat{L}}\left[1 - \left(1 - S_e^{\frac{1}{\mu}}\right)^\mu\right]^2 & \text{if } h \leq 0 \\ K_s & \text{if } h > 0 \end{cases} \tag{5.69}$$

$$C = \begin{cases} -\mu\eta\alpha^\eta \frac{\theta_s - \theta_r}{[1+(\alpha|h|)^\eta]^{\mu+1}}\,|h|^\eta\,h^{-1} & \text{if } h \leq 0 \\ 0 & \text{if } h > 0 \end{cases} \tag{5.70}$$

where $S_e = (\theta - \theta_r)/(\theta_s - \theta_r)$, $\mu = 1 - 1/\eta$, and $\hat{L} = 0.5$. The soil parameters for the MG model are $\theta_s = 0.363$, $\theta_r = 0.186$, $\alpha = 0.01cm^{-1}$, $\eta = 1.53$, and $K_s = 0.0001cm/s$. Initial and boundary conditions are $h(z, t = 0) = -800cm$, $h_{top} = h(100cm, t) = 0cm$, and $h_{bottom} = h(0, t) = -800cm$.

Fig. 13 presents results of the pressure head profile with different grid resolutions for Set 1 using the present numerical approach in comparison with the FDM solution obtained by Celia's h-based method at a dense grid [1]. It can be seen that the numerical results almost coincide as the grid density increases. A similar behaviour is also obtained for the other soil properties associated with Sets 2 and 3 as shown in Figs. 14 and 15, respectively. The

17

solutions obtained by the CIRBF method are in good agreement with the numerical result of Celia et al. [1] and the analytical result of Warrick et al. [38]. We investigate the effect of time step (Δt) on the solutions of the present method and compare the results with those presented by Celia et al. [1] for Set 2. The grid size is taken to be $\Delta z = 2.5cm$. The time step is chosen as $\Delta t = 60.0$, 12.0 and 2.4 minutes. Fig. 16 shows that the present results converge to the dense grid result of Celia et al. faster than those of the FDM when the time step reduces.

5.2. One-dimensional flow in a layered soil

The proposed method is applied to simulate flow in a layered soil for several cases with different values of initial pressure (h_0) and vertical flux at the top of the soil column (q_A) as shown in Table 3. These cases are the same as the ones in the published works [2, 3, 6]. The soil profile has Soil 1 (Berino loamy fine sand) from 0 to $50cm$ and 90 to $100cm$, and Soil 2 (Glendale clay loam) from 50 to $90cm$. The hydraulic parameters of these soils based on the van Genuchten model are presented in Table 4. The simulation time step (Δt) is determined based on an adaptive time-stepping scheme [39, 2] for efficiency and robustness. The time step is increased by 10% if the number of Picard iterations for the previous time step is less than 4 and decreased by 10% if the number of iterations is greater than 8. Fig. 17 presents results of pressure head and volumetric water content with different grid resolutions for Case 1.1 using the FDM and CIRBF scheme. It can be seen that the CIRBF solution converges faster than that of the FDM. The obtained numerical results for all cases at a grid of 101 are in good agreement with those of the FDM and the FVM [6] as shown in Fig. 18.

5.3. Two-dimensional flow in a heterogeneous soil

We simulate the moisture motion in heterogeneous porous media in two dimensions as described in [2]. The computational domain and boundary conditions are illustrated in Fig. 19. All boundaries are non-flow ($q = 0$) except the segment of $100cm$ wide at the top where the vertical flux of $5cm/day$ is applied. The computational region is divided into 9 alternating blocks of Sand and Clay. Sand and Clay are Berino loamy fine sand and Glendale clay loam, respectively.

We apply the proposed numerical approach to solve this problem. Fig. 20 gives the vertical and horizontal fluxes at the cross sections $x = 5cm$ and $z = 95cm$, respectively for different grid sizes and the initial pressure $h_0 =$

18

$-50 \times 10^3 cm$. It is observed that the current numerical results converge to the dense grid solution obtained by the FDM [4] when refining the grid density. At the same grid size of $5cm$, the present result is slightly more accurate than that of the FDM.

The present method is applied to solve the 2–D soil problem for several grid sizes of $\Delta x = \Delta z = \{5.0, 6.25, 10.0, 20.0, 25.0, 50.0\}\, cm$ for the case of $h_0 = -50 \times 10^3 cm$ to investigate how coarse the grid can be before the scheme fails. It appears that the method can yield the solution until the grid size of $25.0cm$ (Figs. 21) and fails at the grid size of $50.0cm$. Fig. 22 illustrates the contours of pressure head at 12.5 days with different grid resolutions of 10.0, 6.25 and 5.0 cm. Figs. 23-25 show the contour of pressure head at several time moments ($t = 1.0,\ 6.0$ and 12.5 days) for different initial pressure heads $h_0 = -10^3 cm, -15 \times 10^3 cm$ and $-50 \times 10^3 cm$, respectively.

For the purpose of CPU time comparisons, we implement the FDM+RFT method to solve the present 2-D soil problem and run all related computations on the same computer. Table 5 shows the CPU time and total number of Picard iterations required for the present CIRBF+RFT simulations in comparison with those of the FDM+RFT simulations. It can be seen that the FDM+RFT method requires less CPU times and number of Picard iterations than the present method.

6. Conclusions

A generalised finite difference approach based on the CIRBF method and the rational function transformation (RFT) method has been successfully developed for simulating the fluid movement in homogeneous and heterogeneous soils. The CIRBF method of a high level of accuracy and fast convergence rate has been demonstrated through the solution of a Poisson equation and a Taylor-Green vortex. When solving the Poisson equation in a non-rectangular domain, the present method performs better than its counterparts (1D-IRBF and MLS-1D-IRBF). The enhanced convergence rate of the present scheme provides an ability to obtain prescribed accuracy faster than the 1D-IRBF and HOC schemes. The numerical results for Poisson equations indicate that the RBF-width parameter β' should be chosen large enough to get high accurate solutions. The value of β' is taken to be 15.0 for solving Taylor-Green vortex and soil problems in the present study. For soil problems, numerical results show that the CIRBF results are more accurate than those of the FDM with second-order central-difference scheme.

19

The CIRBF numerical results obtained for different initial and boundary conditions are in good agreement with other published results in the literature. However, the CIRBF+RFT method consumes more CPU time than the FDM+RFT method because it requires more CPU time for constructing the CIRBF interpolation matrix. Therefore, further study is needed to improve the present scheme in order to reduce the computational cost for solving soil problems.

References

[1] Celia MA, Bouloutas ET, Zarba RL. A general mass-conservative numerical solution for the unsaturated flow equation. *Water Resources Research* 1990; 26 (7):483–1496.

[2] Kirkland MR, Hills RG, Wierenga PJ. Algorithms for solving Richards' equation for variably saturated soils. *Water Resources Research* 1992; 28:2049–2058.

[3] Pan L, Wierenga PJ. A transformed pressure head-based approach to solve Richards' equation for variably saturated soils. *Water Resources Research* 1995; 31(4):925–931.

[4] Pan L, Wierenga PJ. Improving numerical modeling of two-dimensional water flow in variably saturated, heterogenous porous media. *Soil Science Society of America Journal* 1997; 61(2):335–346.

[5] Forsyth PA, Wu YS, Pruess K. Robust numerical methods for saturated–unsaturated flow with dry initial conditions in heterogeneous media. *Advances in Water Resources* 1995; 18:25–38.

[6] McBride D, Cross M, Croft N, Bennett C, Gebhardt J. Computational modelling of variably saturated flow in porous media with complex three-dimensional geometries. *International Journal for Numerical Methods in Fluids* 2006; 50:1085–1117.

[7] Zambra CE, Dumbser M, Toro EF, Moraga NO. A novel numerical method of high-order accuracy for flow in unsaturated porous media. *International Journal for Numerical Methods in Engineering* 2012; 89:227–240.

[8] Caviedes-Voullième D, García-Navarro P, Murillo J. Verification, conservation, stability and efficiency of a finite volume method for the 1D Richards equation. *Journal of Hydrology* 2013; 480:69–84.

[9] Madych WR, Nelson SA. Multivariate interpolation and conditionally positive definite functions. *Approximation Theory and its Applications* 1989; 4:77–89.

[10] Kansa EJ. Multiquadrics - A scattered data approximation scheme with applications to computational fulid-dynamics - I: Surface approximations and partial derivative estimates. *Computers & Mathematics with Applications* 1990; 19(8–9):127–145.

[11] Mai-Duy N, Tran-Cong T. Numerical solution of differential equations using multiquadric radial basis function networks. *Neural Networks* 2001; 14:185–199.

[12] Mai-Duy N, Tanner RI. A collocation method based on one-dimensional RBF interpolation scheme for solving PDEs. *International Journal of Numerical Methods for Heat & Fluid Flow* 2007; 17(2):165–186.

[13] Zerroukat M, Djidjeli K, Charafi A. Explicit and implicit meshless methods for linear advection-diffusion-type partial differential equations. *International Journal for Numerical Methods in Engineering* 2000; 48:19–35.

[14] Lee CK, Liu X, Fan SC. Local multiquadric approximation for solving boundary value problems. *Computational Mechanics* 2003; 30:396–409.

[15] Shu C, Ding H, Yeo KS. Local radial basis function-based differential quadrature method and its application to solve two-dimensional incompressible Navier-Stokes equations. *Computer Methods in Applied Mechanics and Engineering* 2003; 192:941–954.

[16] Ding H, Shu C, Yeo KS, Xu D. Development of least-square-based two-dimensional finite-difference schemes and their application to simulate natural convection in a cavity. *Computers & Fluids* 2004; 33(1):137–154.

[17] Wright GB, Fornberg B. Scattered node compact finite difference-type formulas generated from radial basis functions. *Journal of Computational Physics* 2006; 212:99–123.

[18] Fornberg B, Lehto E. Stabilization of RBF-generated FDMs for convective PDEs. *Journal of Computational Physics* 2011; 230:2270–2285.

[19] Flyer N, Fornberg B, Bayona V, Barnett GA. On the role of polynomials in RBF-FD approximations: I. Interpolation and accuracy. *Journal of Computational Physics* 2016; 321:21–38.

[20] Vertnik R, Šarler B. Meshless local radial basis function collocation method for convective-diffusive solid-liquid phase change problems. *International Journal of Numerical Methods for Heat & Fluid Flow* 2006; 16:617–640.

[21] Stevens D, Power H, Lees M, Morvan H. The use of PDE centres in the local RBF Hermitian method for 3D convective-diffusion problems. *Journal of Computational Physics* 2009; 228:4606–4624.

[22] Jackson SJ, Stevens D, Giddings D, Power H. An adaptive RBF finite collocation approach to track transport processes across moving fronts. *Computers & Mathematics with Applications* 2016; 71(1):278–300.

[23] An-Vo DA, Mai-Duy N, Tran-Cong T. A C2-continuous control-volume technique based on cartesian grids and two-node integrated-rbf elements for second-order elliptic problems. *Computer Modeling in Engineering & Sciences* 2011; 72(4):299–334.

[24] An-Vo DA, Mai-Duy N, Tran-Cong T. High-order upwind methods based on C 2-continuous two-node integrated-RBF elements for viscous flows. *Computer Modeling in Engineering & Sciences* 2011; 80 (2):141–177.

[25] An-Vo DA, Tran C-D, Mai-Duy N, Tran-Cong T. RBF-based multiscale control volume method for second order elliptic problems with oscillatory coefficients. *Computer Modeling in Engineering & Sciences* 2012; 89(4):303–359.

[26] Ngo-Cong D, Mai-Duy N, Karunasena W, Tran-Cong T. Local Moving Least Square - One-Dimensional IRBFN Technique for Incompressible

Viscous Flows. *International Journal for Numerical Methods in Fluids* 2012; 70:1443–1474.

[27] Mai-Duy N, Tran-Cong T. Compact local integrated-RBF approximations for second-order elliptic differential problems. *Journal of Computational Physics* 2011; 230:4772–4794.

[28] Mai-Duy N, Tran-Cong T. A compact five-point stencil based on integrated RBFs for 2D second-order differential problems. *Journal of Computational Physics* 2013; 235:302–321.

[29] Thai-Quang N, Le-Cao K, Mai-Duy N, Tran C-D, Tran-Cong T. A numerical scheme based on compact integrated-RBFs and Adams-Bashforth/Crank-Nicolson algorithms for diffusion and unsteady fluid flow problems. *Engineering Analysis with Boundary Elements* 2013; 37(12):1653–1667.

[30] Hardy RL. Theory and applications of the multiquadric-biharmonic method. *Computers & Mathematics with Applications* 1990; 8-9:163–208.

[31] Sarra SA. Integrated multiquadric radial basis function approximation methods. *Computers & Mathematics with Applications* 2006; 51:1283–1296.

[32] Tien CMT, Thai-Quang N, Mai-Duy N, Tran C-D, Tran-Cong T. High-order fully coupled scheme based on compact integrated RBF approximation for viscous flows in regular and irregular domains. *Computer Modeling in Engineering & Sciences* 2015; 105:301–340.

[33] Ngo-Cong D, Mai-Duy N, Karunasena W, Tran-Cong T. Local Moving Least Square - One-Dimensional IRBFN Technique: Part I - Natural Convection Flows in Concentric and Eccentric Annuli. *Computer Modeling in Engineering & Sciences* 2012; 83(3): 275–310.

[34] Tian Z, Liang X, Yu P. A higher order compact finite difference algorithm for solving the incompressible Navier Stokes equations. *International Journal for Numerical Methods in Engineering* 2011; 88:511–532.

[35] Hanby RF, Silvester DJ, Chew JW. A comparison of coupled and segregated iterative solution techniques for incompressible swirling flow. *International Journal for Numerical Methods in Fluids* 1996; 22:353–373.

[36] Mazhar Z. A procedure for the treatment of the velocity-pressure coupling problem in incompressible fluid flow. *Numerical Heat Transfer, Part B: Fundamentals: An International Journal of Computation and Methodology* 2001; 39(1):91–100.

[37] Haverkamp R, Vauclin M, Touma J, Wierenga PJ, Vachaud G. A comparison of numerical simulation models for one-dimensional infiltration. *Soil Science Society of America Journal* 1977; 41:285–294.

[38] Warrick AW, Lomen DO, Yates SR. A generalized solution to infiltration. *Soil Science Society of America Journal* 1985; 49(1):34–38.

[39] Bouloutas ET. 1989. *Improved numerical methods for modeling flow and transport processes in partially saturated porous media.* Massachusetts Institute of Technology, Department of Civil Engineering.

Table 1: Poisson equation: grid convergence study of RMS for the present CIRBF method ($\beta' = 25$) in comparison with the FDM, 1D-IRBF and HOC methods.

Grid	FDM	1D-IRBF	HOC	Present CIRBF
21×21	8.9109E-03	5.8623E-04	3.3579E-04	3.3220E-04
31×31	3.9994E-03	1.7845E-04	5.6856E-05	5.5507E-05
41×41	2.2630E-03	7.6214E-05	1.4589E-05	1.4036E-05
51×51	1.4540E-03	3.9174E-05	4.9330E-06	4.6891E-06
61×61	1.0125E-03	2.2653E-05	2.0151E-06	1.9215E-06
71×71	7.4536E-04	1.4215E-05	9.4467E-07	9.4341E-07
Convergence rate	$O(g^{2.036})$	$O(g^{3.052})$	$O(g^{4.837})$	$O(g^{4.847})$

Table 2: Taylor-Green vortex: grid convergence study of numerical results at $t = 2.0$ for the present CIRBF-Fully Coupled ($\beta' = 15$) in comparison with the HOC-Fully Coupled and HOC-Fractional [34].

	Present CIRBF-Fully Coupled		
Grid	u-error	v-error	p-error
11×11	1.5214251E-01	1.5218216E-01	5.3403483E-01
21×21	3.9925074E-03	3.9924747E-03	2.1199636E-02
31×31	3.2600624E-04	3.2600469E-04	5.1768763E-03
41×41	2.8866736E-05	2.8866407E-05	6.0032401E-04
51×51	1.4292601E-05	1.4292574E-05	4.2213874E-04
Rate	$O(g^{5.96})$	$O(g^{5.96})$	$O(g^{4.56})$
	HOC-Fully Coupled		
Grid	u-error	v-error	p-error
11×11	1.8156049E-01	1.8156049E-01	3.0412542E-01
21×21	4.5719207E-03	4.5719207E-03	8.5425929E-03
31×31	5.0521189E-04	5.0521191E-04	2.6558403E-03
41×41	1.0478762E-04	1.0478758E-04	3.4579194E-04
51×51	3.0814364E-05	3.0814437E-05	2.6395965E-04
Rate	$O(g^{5.39})$	$O(g^{5.39})$	$O(g^{4.47})$
	HOC-Fractional [34]		
Grid	u-error	v-error	p-error
11×11	7.0070489E-02	7.0070489E-02	1.0764149E-01
21×21	9.0692193E-03	9.0692193E-03	1.0567607E-02
31×31	2.8851487E-03	2.8851487E-03	2.9103288E-03
41×41	1.2238736E-03	1.2238736E-03	1.1356134E-03
51×51	6.3063026E-04	6.3063026E-04	5.3933641E-04
Rate	$O(g^{2.92})$	$O(g^{2.92})$	$O(g^{3.28})$

Table 3: One-dimensional flow in a layered soil: initial and boundary conditions, elapsed times. h_0 is the initial pressure, and q_A and q_C denote for the vertical flux at the top and bottom of the soil column, respectively.

Case	$h_0(cm)$	$q_A(cm/h)$	$q_C(cm/h)$	Elapsed time (h)
1.1	-200	0.3	0	4.0
1.2	-1000	0.3	0	8.0
1.3	-50000	0.3	0	12.0
2.1	-200	1.25	0	3.8
2.2	-1000	1.25	0	5.0
2.3	-50000	1.25	0	6.0

Table 4: Hydraulic parameters of Soils 1 and 2 in a layered soil.

Parameters	Soil 1	Soil 2
θ_s	0.3658	0.4686
θ_r	0.0286	0.1060
$\alpha(cm^{-1})$	0.0280	0.0104
$\hat{\eta}$	2.2390	1.3954
$K_s(cm/h)$	22.54	0.5458

Table 5: 2-D soil problem: comparisons (between the present CIRBF+RFT and FDM+RFT) of CPU time and total number of Picard iterations ($N_{iteration}$) required for simulations with different initial pressure heads (h_0) and several grid sizes ($\Delta x = \Delta z$).

$h_0(cm)$	Method	Grid size (cm)	CPU time (s)	$N_{iteration}$
-1000	FDM+RFT	20.00	17.2	1449
		10.00	301.3	2362
		6.25	2910.9	3845
		5.00	8776.6	4876
	CIRBF+RFT	20.00	68.1	2514
		10.00	2296.0	5459
		6.25	28481.1	10057
		5.00	107098.0	13278
-15000	FDM+RFT	20.00	18.7	1497
		10.00	290.6	2381
		6.25	3389.7	4044
		5.00	9235.0	4995
	CIRBF+RFT	20.00	70.0	2595
		10.00	2380.3	5584
		6.25	32343.2	10333
		5.00	110045.6	13520
-50000	FDM+RFT	20.00	17.5	1230
		10.00	284.6	2571
		6.25	3345.1	4130
		5.00	7841.0	5110
	CIRBF+RFT	20.00	79.7	2639
		10.00	2100.5	5750
		6.25	30612.9	9579
		5.00	119663.7	13652
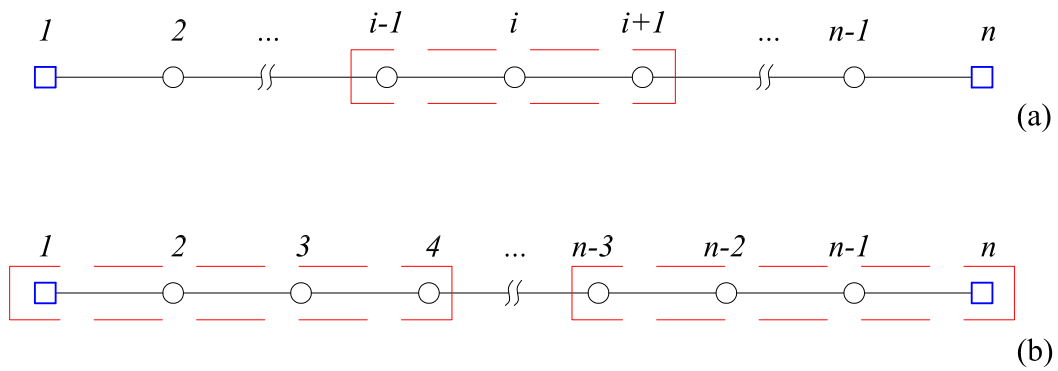
Fig. 1: Schematic outline of (a) a 3-point CIRBF stencil for interior nodes and (b) 4-point CIRBF stencils for two boundary nodes.
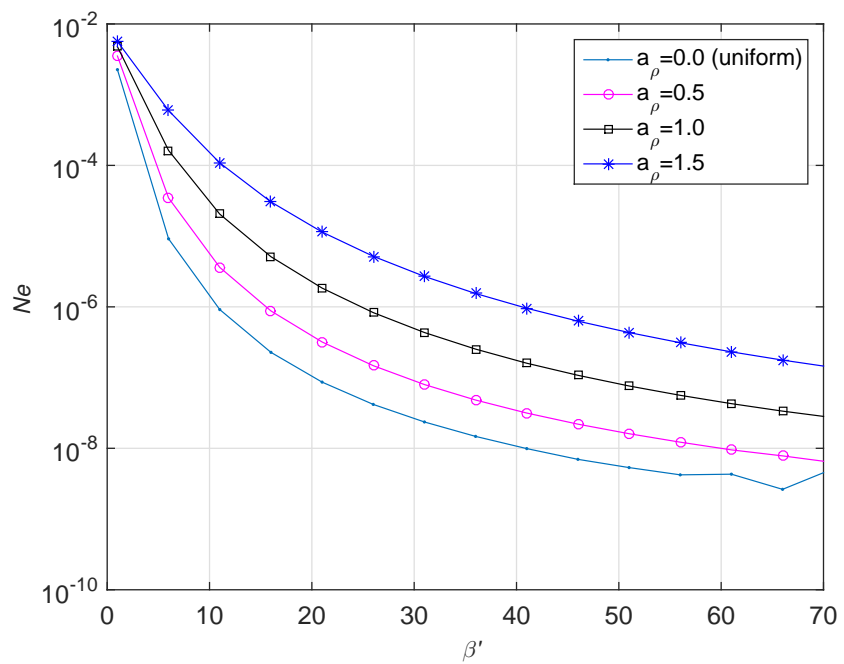
Fig. 2: ODE-1: the solution accuracy (Ne) against the RBF width (β') for four different distributions of collocations points, $N = 501$.
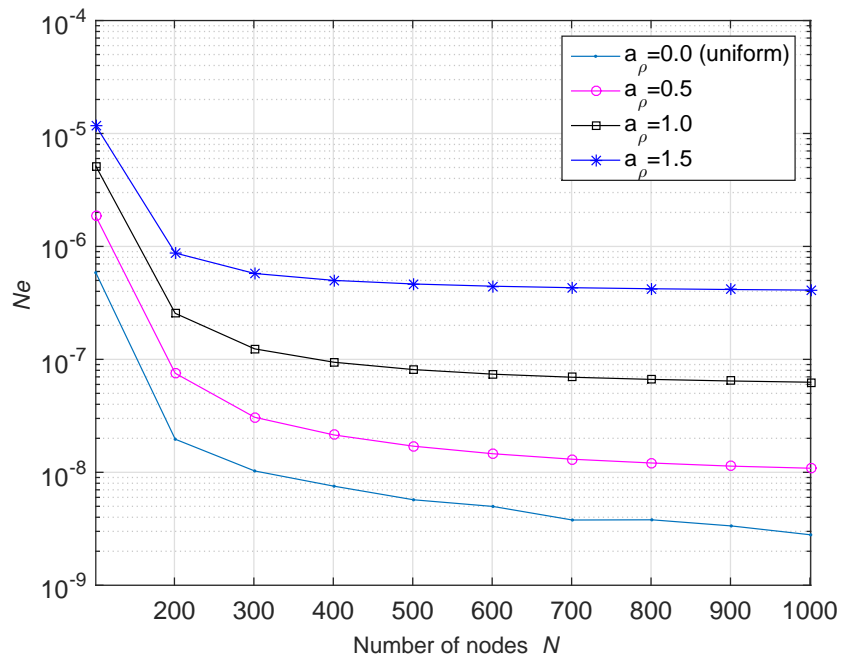
Fig. 3: ODE-1: the solution accuracy (Ne) against the number of grids (N) for four different distributions of collocations points, $\beta' = 50$.
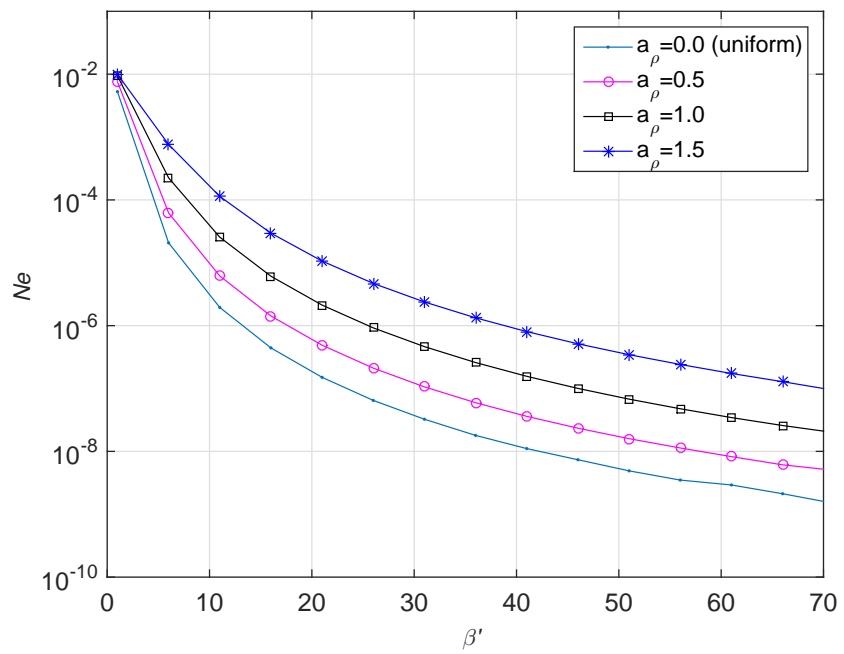
Fig. 4: ODE-2: the solution accuracy (Ne) against the RBF width (β') for four different distributions of collocations points, $N = 501$.
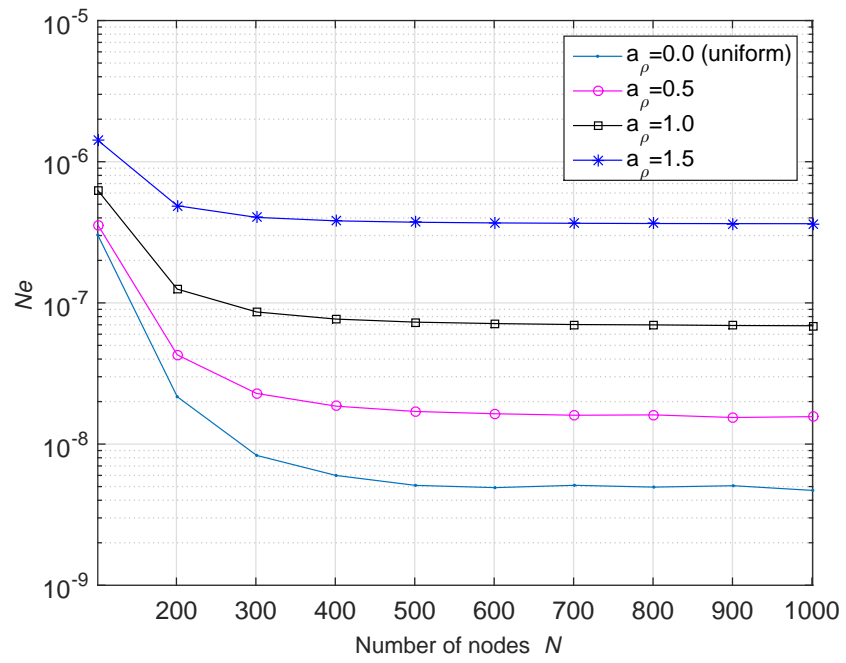
Fig. 5: ODE-2: the solution accuracy (Ne) against the number of grids (N) for four different distributions of collocations points, $\beta' = 50$.
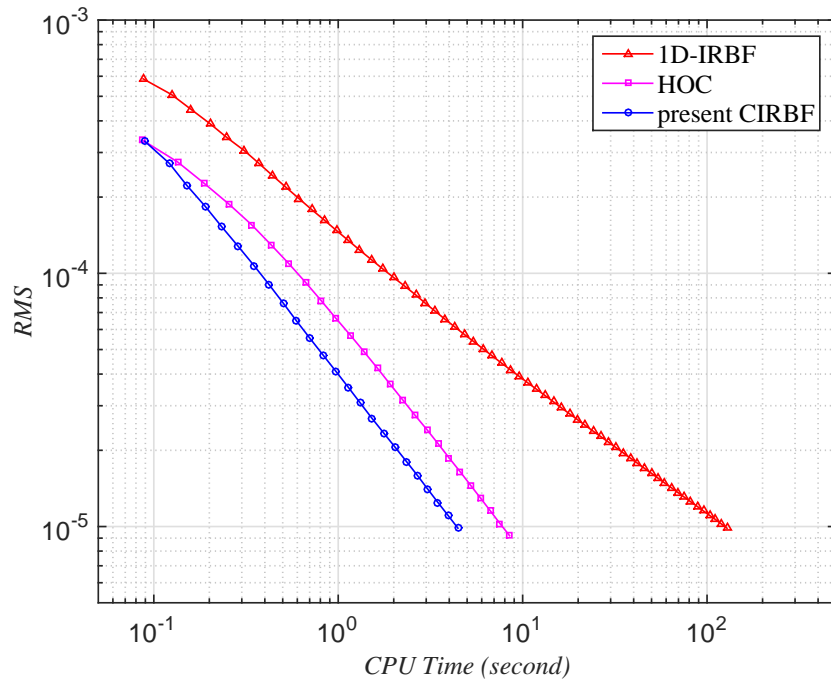
Fig. 6: Poisson equation: comparison of computational cost of the present CIRBF, 1D-IRBF and HOC schemes. The grid size increases as $\{21 \times 21, 22 \times 22, ...\}$ until the solution accuracy achieves a target RMS level of 10^{-5}. The final grid sizes for the 1D-IRBF, HOC and present CIRBF are, respectively, 81×81, 45×45 and 44×44.
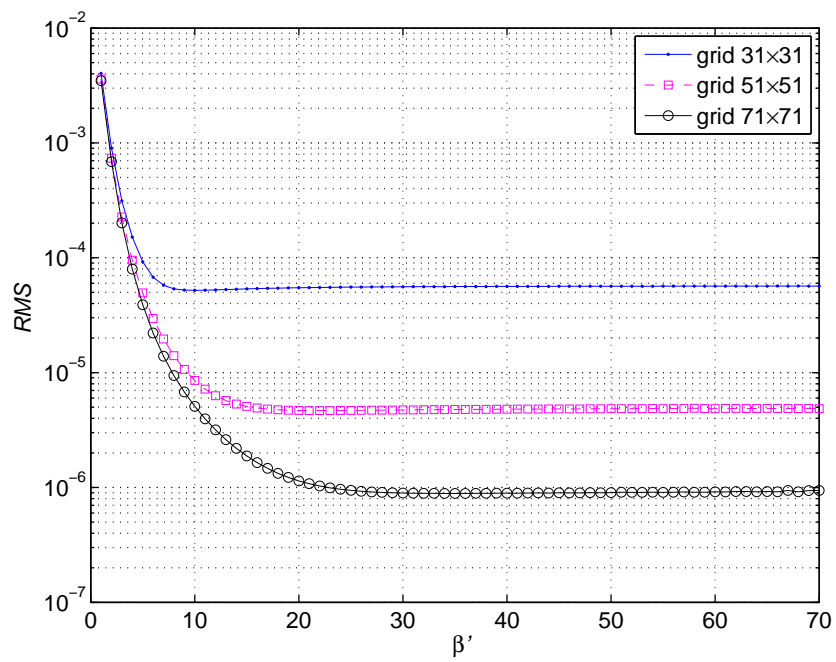
Fig. 7: Poisson equation: the solution accuracy (RMS) against the RBF width (β') for three different grids.
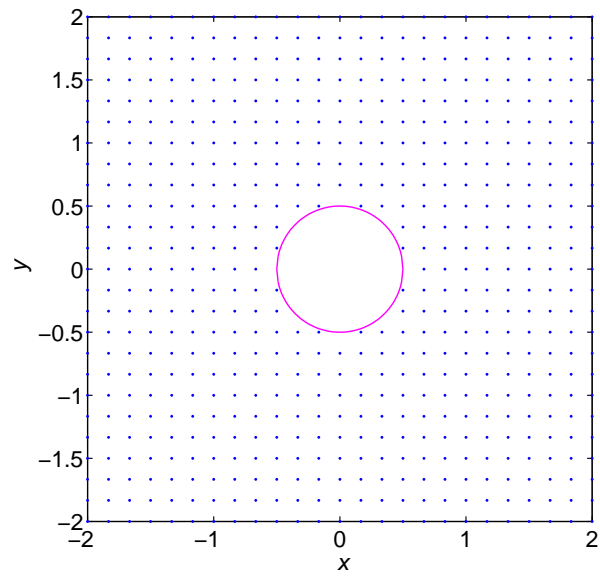
Fig. 8: A square domain with a circular hole.
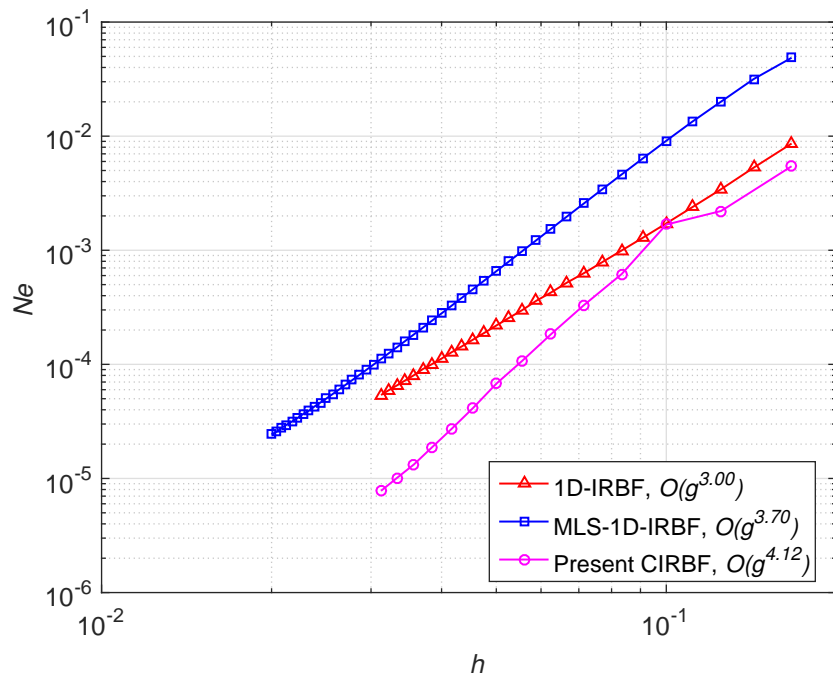
Fig. 9: Poisson in a square domain with a circular hole: grid convergence study for the 1D-IRBF, MLS-1D-IRBFN-5-node and present CIRF methods, with $\beta' = 15$.
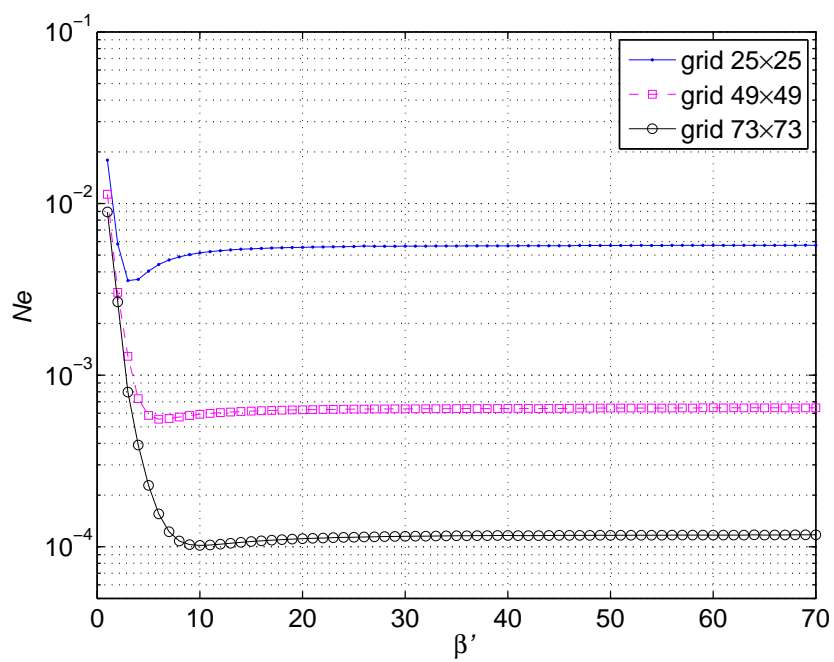
Fig. 10: Poisson in a square domain with a circular hole: the solution accuracy (Ne) against the RBF width (β') for three different grids.
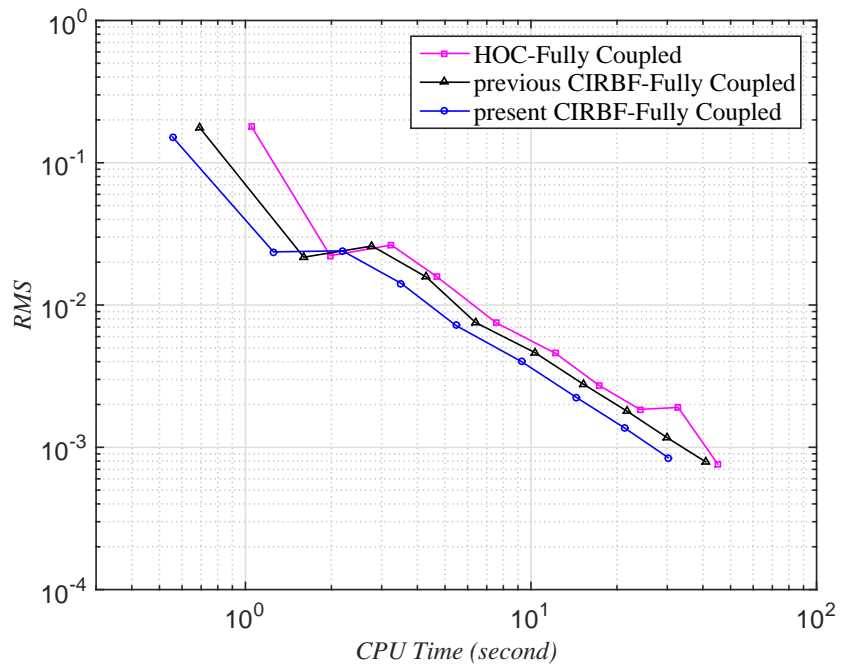
Fig. 11: Taylor-Green vortex: comparison of computational cost of the present CIRBF and HOC schemes. The grid size increases as $\{11 \times 11, 13 \times 13, ...\}$ until the solution accuracy of the u-velocity achieves a target RMS level of 10^{-3}. The final grid sizes for the HOC, previous CIRBF and present CIRBF are, respectively, 29×29, 29×29 and 27×27.
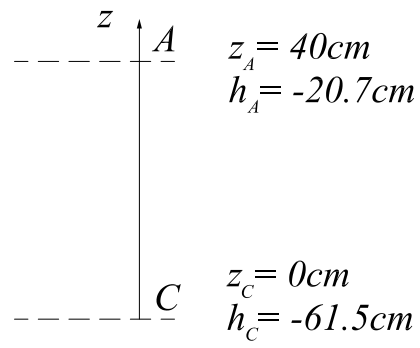
Fig. 12: 1-D soil problem: Geometry and boundary conditions.
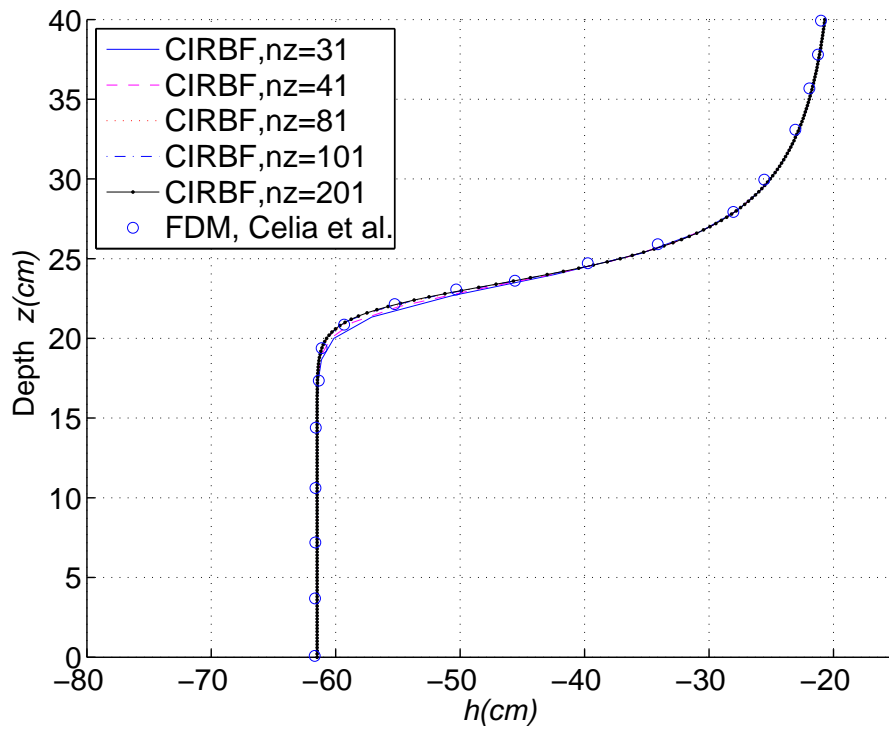
Fig. 13: 1-D soil problem (Set 1): results of pressure head at time $t = 360s$, using RFT method in conjunction with CIRBF scheme, and $\Delta t = 1s$.
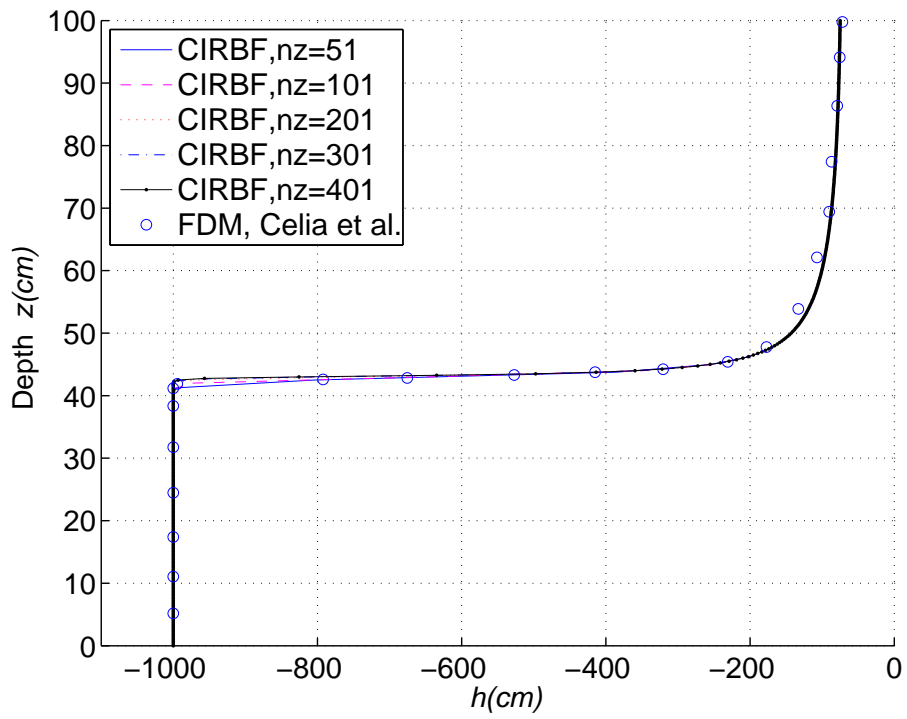
Fig. 14: 1-D soil problem (Set 2): results of pressure head at time $t = 1day$, using RFT method in conjunction with CIRBF scheme, and $\Delta t = 1min$.
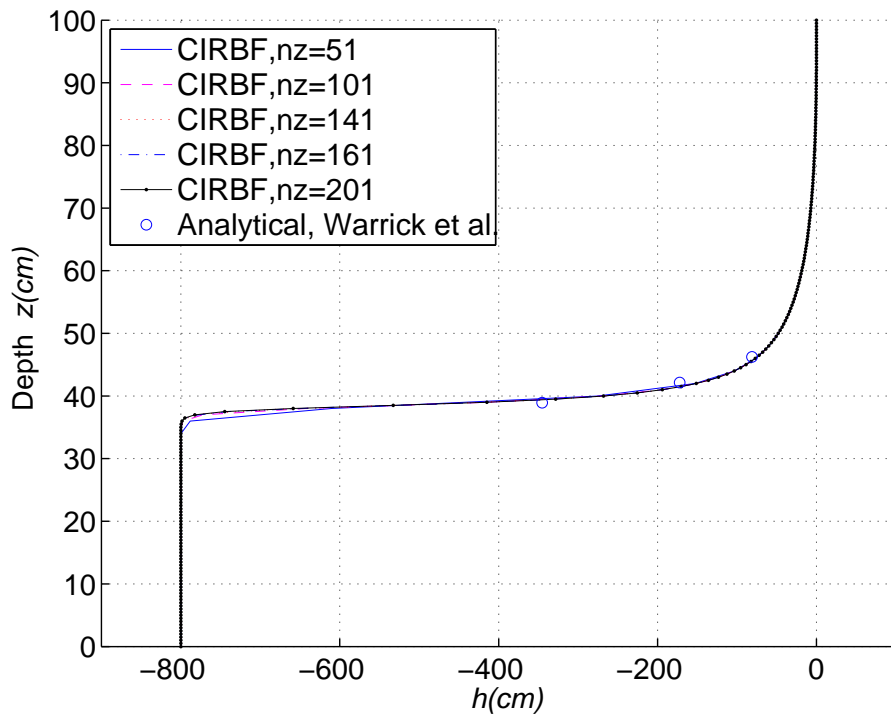
Fig. 15: 1-D soil problem (Set 3): results of pressure head at time $t = 13h$, using RFT method in conjunction with CIRBF scheme, and $\Delta t = 0.5min$.
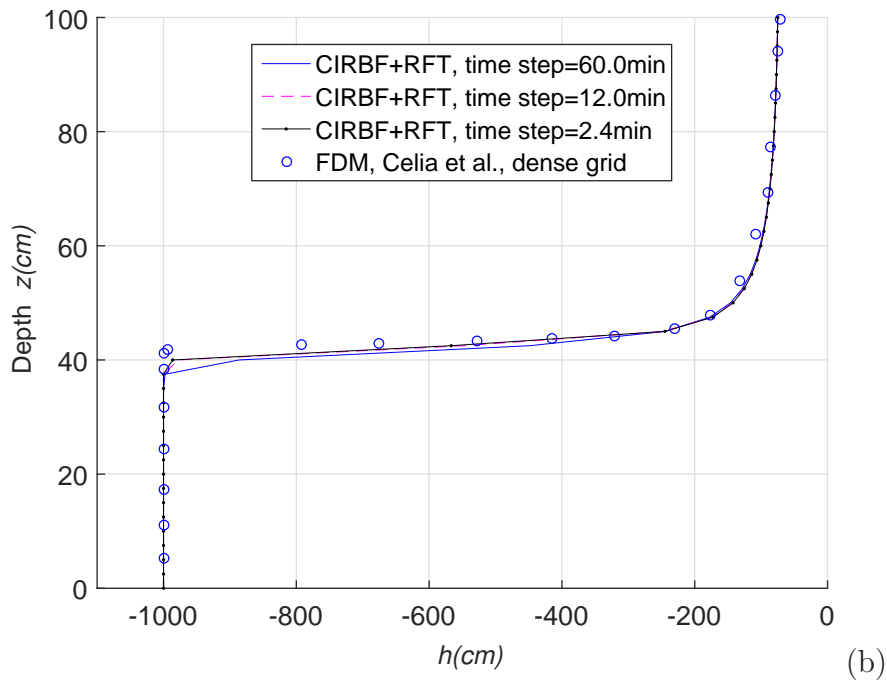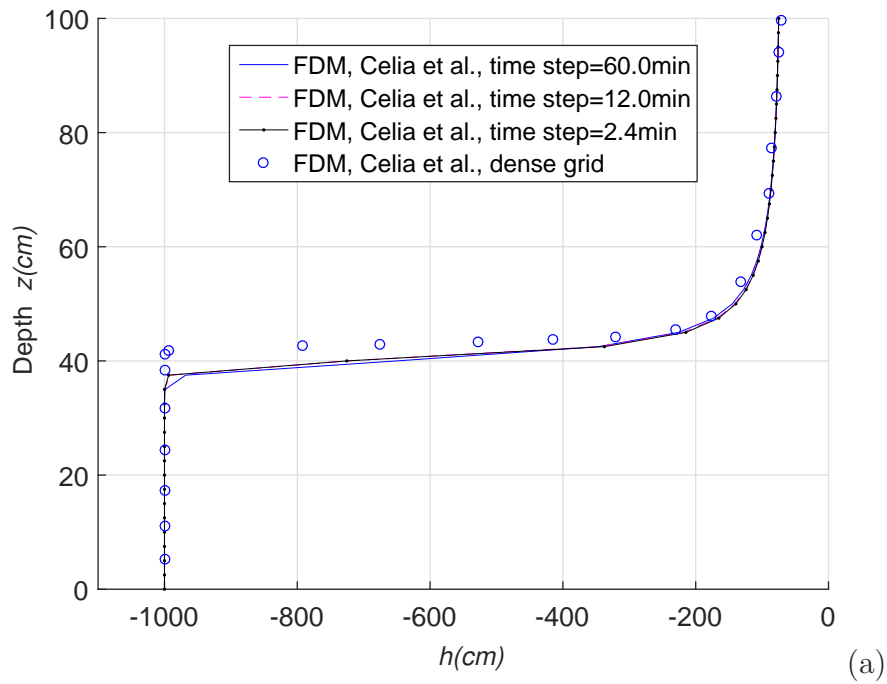
Fig. 16: 1-D soil problem (Set 2): results for different time steps, at time $t = 1day$, using a grid size $\Delta z = 2.5cm$, and (a) Celia et al.'s method, (b) CIRBF+RFT method.
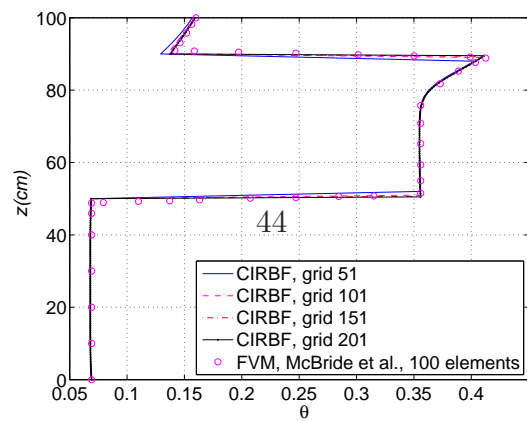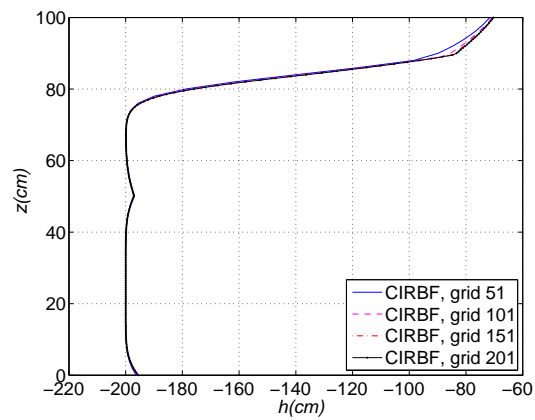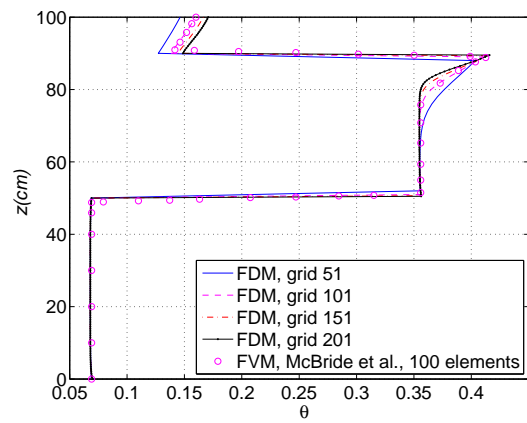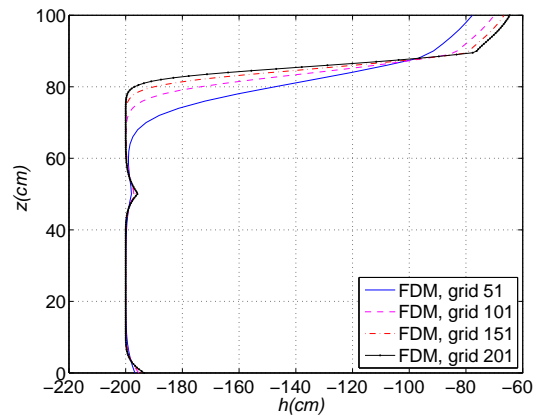
Fig. 17. 1-D flow in layered soil: results for pressure head h (left) and water content θ

$q_A = 0.3cm/h$ $q_A = 1.25cm/h$

45
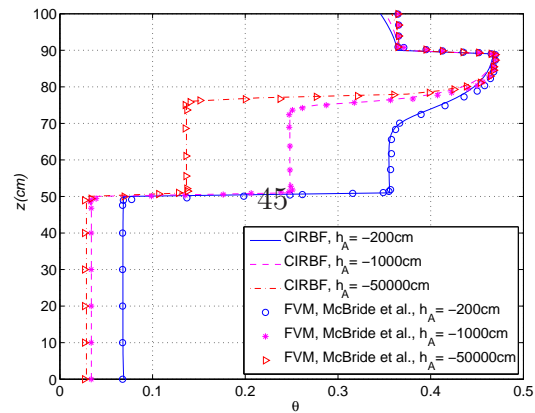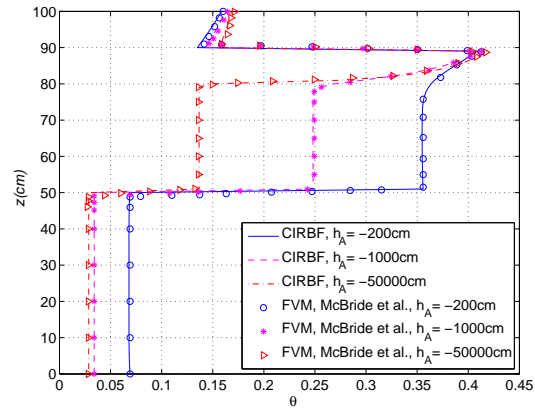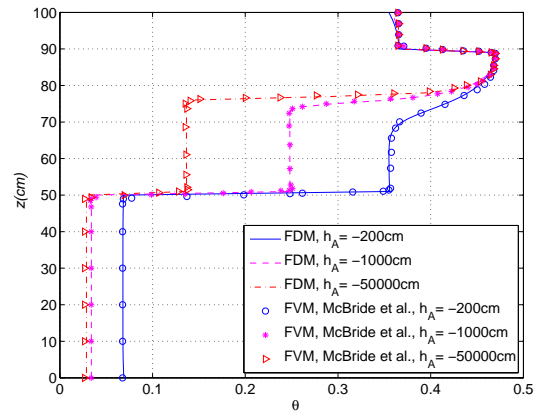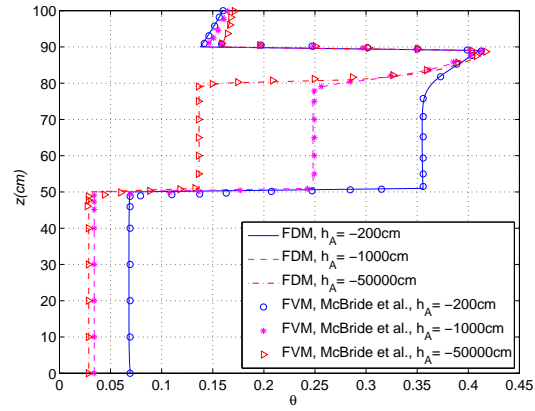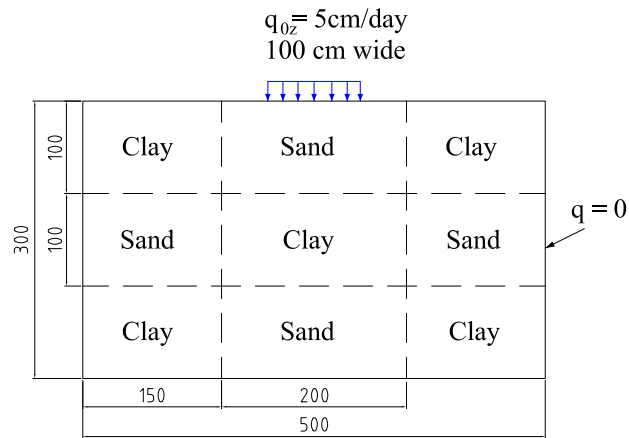
Fig. 19: 2-D soil problem: geometry and boundary conditions. The infiltration process into a very dry region which is divided into 9 alternating blocks of sand and clay.
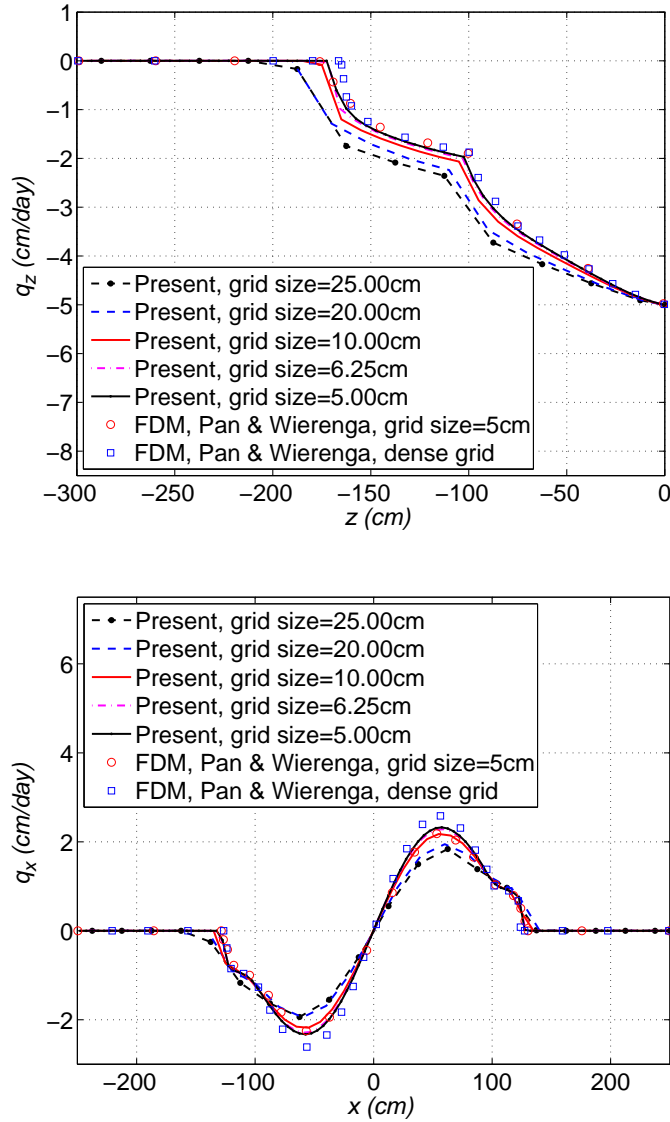
Fig. 20: 2-D soil problem: results of vertical flux q_z at $x = 5cm$ (top) and horizontal flux q_x at $y = 95cm$ (bottom) for several grid resolutions, at time $t = 12.50$ days, for $h_0 = -50 \times 10^3 cm$, $q_{0z} = 5cm/day$, using the CIRBF scheme in conjunction with the RFT method.
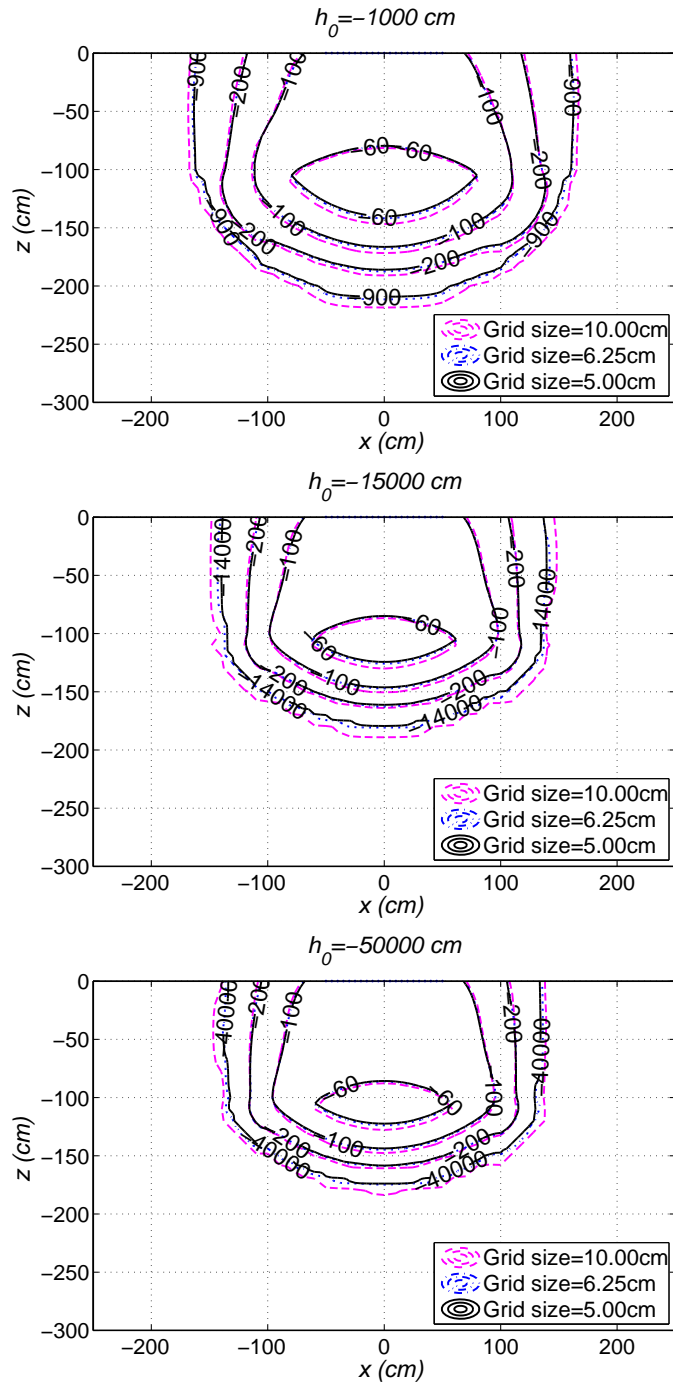
47
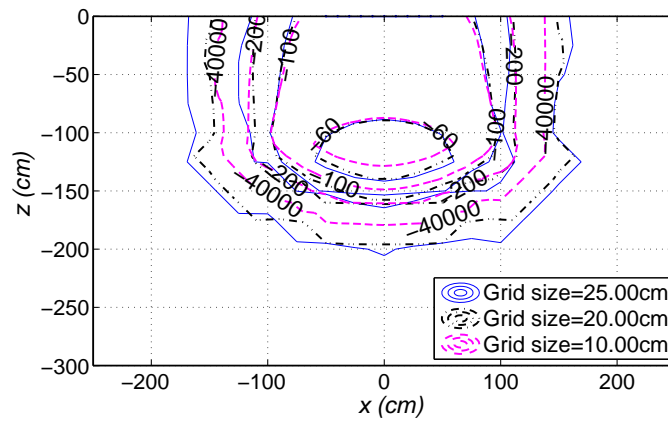
Fig. 21: 2-D soil problem: contours of pressure head $h(cm)$ at $t = 12.50$ days, using the CIRBF scheme in conjunction with the RFT method, and different grid sizes $\Delta x = \Delta z = \{25,\ 20,\ 10\}cm$, for $h_0 = -50 \times 10^3 cm$.

Fig. 22: 2-D soil problem: contours of pressure head $h(cm)$ at $t = 12.50$ days, using the CIRBF scheme in conjunction with the RFT method, and different grid sizes $\Delta x = \Delta z = \{10, 6.25, 5\}cm$, for different initial pressure heads.
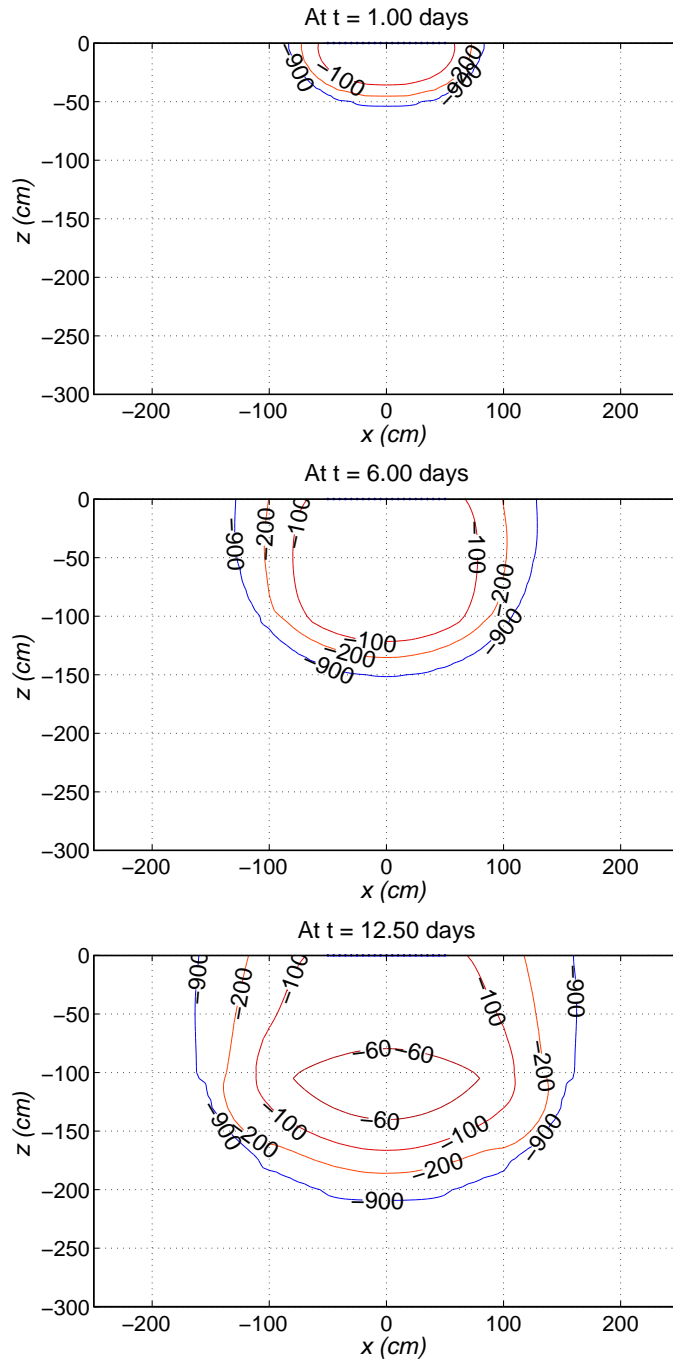
Fig. 23: 2-D soil problem: contours of pressure head $h(cm)$ at different times t for $h_0 = -10^3 cm$, $q_{0z} = 5cm/day$, using the CIRBF scheme in conjunction with the RFT method, and a grid size of $5cm$.
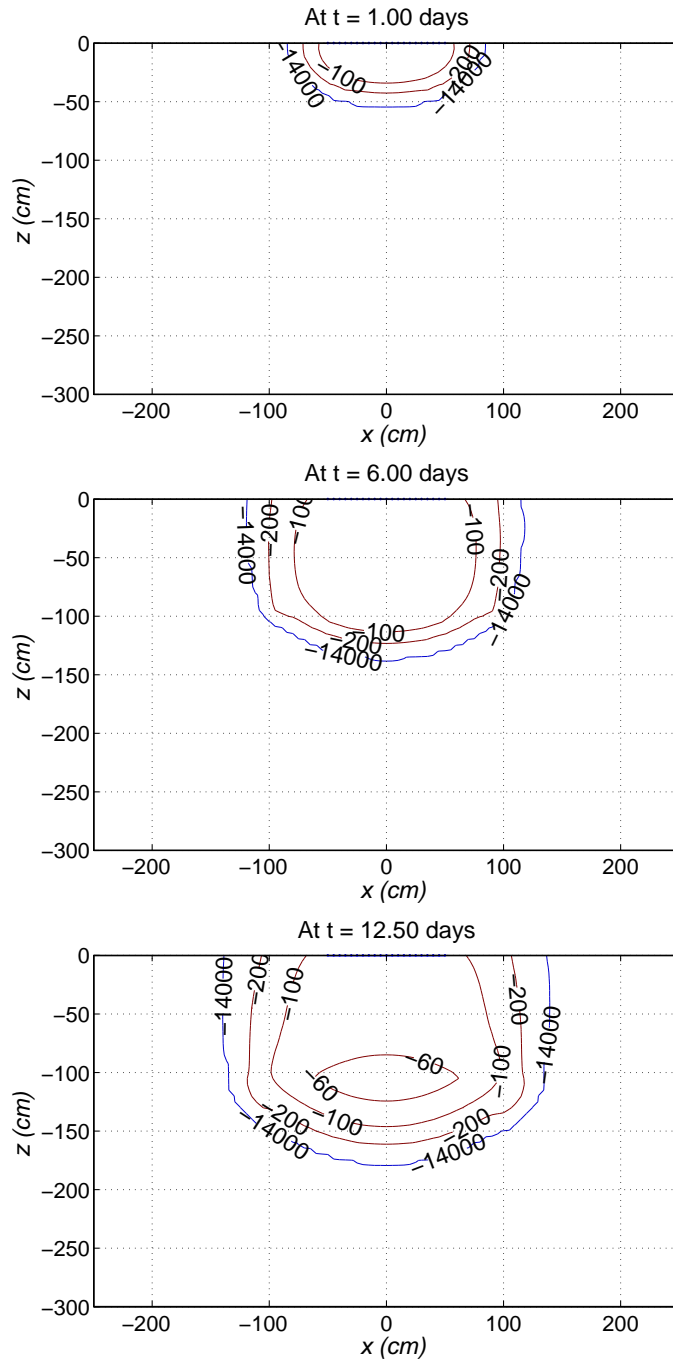
50

Fig. 24: 2-D soil problem: contours of pressure head $h(cm)$ at different times t for $h_0 = -15 \times 10^3 cm$, $q_{0z} = 5 cm/day$, using the CIRBF scheme in conjunction with the RFT method, and a grid size of $5cm$.
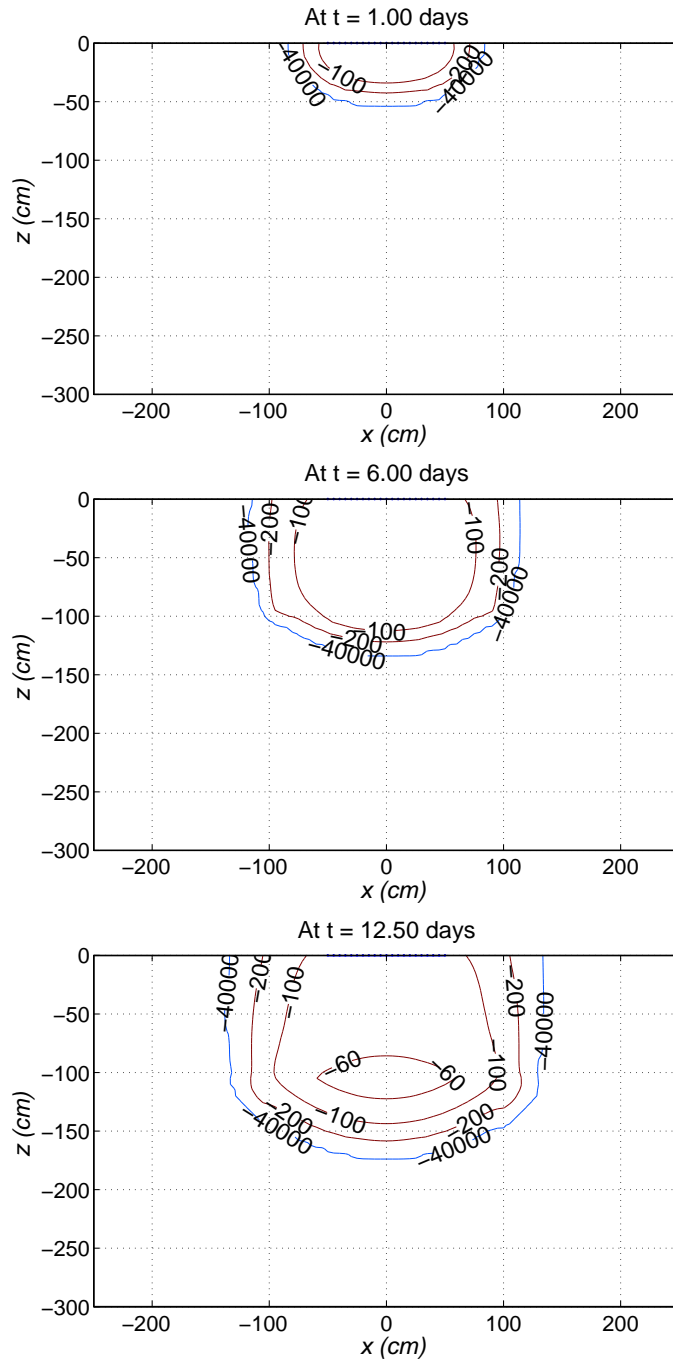
51

Fig. 25: 2-D soil problem: contours of pressure head $h(cm)$ at different times t for $h_0 = -50 \times 10^3 cm$, $q_{0z} = 5cm/day$, using the CIRBF scheme in conjunction with the RFT method, and a grid size of $5cm$.